various types of Pax5 transcripts. Sequencing analysis of several cDNA clones revealed that there are three types of cDNA encoding distinct C-terminal amino acid sequences. We designated those as wt (wild type), del9 (deletion of exon 9) and ins8′ (insertion of novel exon 8′), respectively. One skips exon 9 without subsequent frameshift (del9), and the other has a 154 bp insert between exons 8 and 9 (ins8′), resulting in novel C-terminal sequences by frameshift (Fig. 1A). By homology search using BLAST program, this 154 bp insert was confirmed to be derived from the genomic region between exons 8 and 9 of the human Pax5 gene [19] as shown in Fig. 1A. Such a complex pattern of alternative splicing is likely to occur at the C-terminus of the Pax2/5/8 gene family as reported [20,21].

To gain insight into the role of Pax5 isoforms during human early B cell differentiation, we conducted quantitative measurement of each transcript using primers and probes designed for Taqman assay (Fig. 2A). As shown in Fig. 2B, wt mRNA could be detected in CB CD34$^+$ cells, but transcripts for del9 and ins8′ isoforms only appeared after 1 or 3 weeks of co-culture, respectively (Fig. 2B). Expression of each isoform mRNA was markedly (10^3- to 10^4-fold) upregulated in a similar time-dependent manner during the culture until the 6th week, and was slightly reduced at the 7th week. Wt mRNA continued to be much more abundant than del9 and ins8′ throughout the culture periods. Since purified CD34$^+$ cells are still heterogeneous in the differentiation stage and the lineage commitment, detection of small amounts of Pax5 transcripts in CB CD34$^+$ cells means that Pax5$^+$CD34$^+$ early B cell progenitors occupy a very limited part of this population. In contrast, adherent cells during the culture are relatively homogeneous populations already committed to the B cell lineage. This result suggests that only Pax5-wt may be expressed by most primitive committed B cell progenitors and that splicing of C-terminal exons may be developmentally regulated.

To confirm the protein product of each Pax5 isoform cDNA, the lysates prepared from 293T cells transfected with pcDNA-Pax5 were subjected to immunoblot analysis using antibody against N-terminal portion of human Pax5. Expression of each Pax5 isoform cDNA resulted in the expected molecular mass of 48 kDa (wt and ins8′) and 43 kDa (del9), respectively, shown in Fig. 3A. Transactivation potential of each Pax5 isoform was tested in two distinct assays. At first, a conventional luciferase reporter assay was performed with a plasmid containing high-affinity Pax5 binding sites of the human CD19 gene (Fig. 3B)

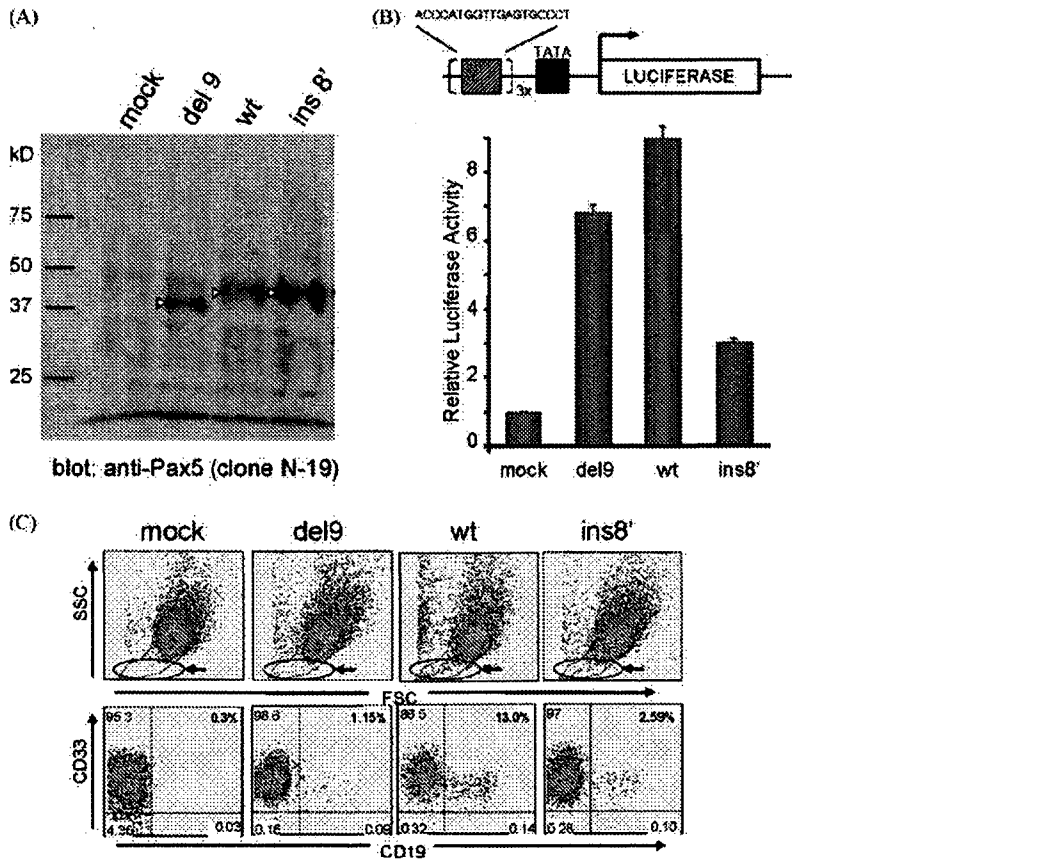

Fig. 3. Functional analysis of Pax5 isoforms. (A) Immunoblot analysis of Pax5 isoforms: arrows indicate the molecular mass corresponding to each isoform. (B) (Upper) Scheme of CD19-Luc reporter vector. BSAP sequence indicates a single copy of the high-affinity binding site for Pax5, and TATA means a minimal promoter. (Lower) Transcriptional activity of each Pax5 isoform. The results indicate the mean ± S.D. in triplicate assays and are shown as fold induction compared with mock vector. (C) Flow cytometry of non-adherent cells after 1 week culture of CD34$^+$ cells. A minor but significant part of Pax5-transduced cells appeared in the circled areas indicated by arrows (lymphoid gate). Induction of aberrant CD19 expression on CD33$^+$ non-adherent cells transduced with Pax5 isoforms.

in Hela cells, which lack endogenous Pax5. As a result, Pax5-wt induced ninefold higher luciferase activity compared with vector control, whereas del9 and ins8′ isoform revealed seven- and threefold induction, respectively (Fig. 3B). Robichaud et al. also reported that del9 isoform is slightly less potent than Pax5-wt in transfection experiments with a similar reporter plasmid [11].

Next, $CD34^+$ cells were retrovirally transduced with Pax5 isoforms, and were subjected to the co-culture assay after sorting on FACS. $EGFP^+$ cell fractions were usually more than 95% pure upon reanalysis. After 1 week, a minor but significant fraction of non-adherent cells could be detected in the lymphoid gate of the cell population transduced with Pax5 isoforms but not vector control, and these cell populations were positive for both CD19 and CD33 (Fig. 3C). However, $CD19^+CD33^+$ cells appeared transiently and could not be detected after 2 weeks of culture (data not shown). The relative EGFP fluorescence intensity (FI) of these populations, which is likely to reflect Pax5 expression, is comparable to each other among Pax5 isoforms (mean FI = ~50). The average ratio of $CD19^+CD33^+$ cell population at Day 7 induced by Pax5-wt was 10.14% in three independent experiments and much more prominent than del9 (1.23%) and ins8′ (2.60%), suggesting its most potent transcriptional activity of the CD19 gene in this cell context (Fig. 3C). Curiously, ins8′ isoform appears more potent than del9 in this assay, which is inconsistent with the result in Fig. 3B. This may be partly attributed to the distinction in the target genes between both assays; CD19-Luc for luciferase assay and the native CD19 gene for FACS assay. Using a series of C-terminal deletion mutants of Pax5, Busslinger and co-worker identified both transactivation and inhibitory domains in the C-terminal region of Pax5 depicted in Fig. 1B [12]. Our data is not conflicting with their results. Human Pax5 is well known to have multiple and complex pattern of isoforms due to alternative splicing [10,11], and this phenomenon tends to be associated with neoplastic transformation of B lymphoid cells.

The present study demonstrated the presence of C-terminal isoforms of Pax5 in primary human B cell progenitors for the first time and confirmed the predominance of Pax5-wt over other C-terminal isoforms (del9 and ins8′) in quantitative and qualitative aspects, although the physiological significance of these minor isoforms still remains to be elucidated. We also developed a novel assay system for transactivation potential of Pax5 by flow cytometric analysis of virally transduced CB $CD34^+$ cells in the co-culture with HESS-5 cells. This assay system can be applied to other transcription factors required for B cell as well as myeloid cell development.

Acknowledgements

This study is supported in part by a Grant-in-aid from the Ministry of Education, Science, Sports, and Culture of Japan. We thank to Asuka Tajima for technical assistance and the Tokyo Cord Blood Bank for cord blood samples.

References

[1] Schebesta M, Heavey B, Busslinger M. Transcriptional control of B-cell development. Curr Opin Immunol 2002;14:216–23.
[2] Nutt SL, Heavey B, Rolink AG, Busslinger M. Commitment to the B-lymphoid lineage depends on the transcription factor Pax5. Nature 1999;401:556–62.
[3] Urbanek P, Wang ZQ, Fetka I, Wagner EF, Busslinger M. Complete block of early B cell differentiation and altered patterning of the posterior midbrain in mice lacking Pax5/BSAP. Cell 1994;79:901–12.
[4] Mikkola I, Heavey B, Horcher M, Busslinger M. Reversion of B cell commitment upon loss of Pax5 expression. Science 2002;297:110–3.
[5] Chiang MY, Monroe M. BSAP/Pax5A expression blocks survival and expansion of early myeloid cells implicating its involvement in maintaining commitment to the B-lymphocyte lineage. Blood 1999;94:3621–32.
[6] Chiang MY, Monroe JG. Role for transcription Pax5A factor in maintaining commitment to the B cell lineage by selective inhibition of granulocyte-macrophage colony-stimulating factor receptor expression. J Immunol 2001;166:6091–8.
[7] Souabni A, Cobaleda C, Schebesta M, Busslinger M. Pax5 promotes B lymphopoiesis and blocks T cell development by repressing Notch1. Immunity 2002;17:781–93.
[8] Zwollo P, Arrieta H, Ede K, Molinder K, Desiderio S, Pollock R. The Pax-5 gene is alternatively spliced during B-cell development. J Biol Chem 1997;272:10160–8.
[9] Busslinger M, Klix N, Pfeffer P, Graninger PG, Kozmik Z. Deregulation of PAX-5 by translocation of the Emu enhancer of the IgH locus adjacent to two alternative PAX-5 promoters in a diffuse large-cell lymphoma. Proc Natl Acad Sci USA 1996;93:6129–34.
[10] Borson ND, Lacy MQ, Wettstein PJ. Altered mRNA expression of Pax5 and Blimp-1 in B cells in multiple myeloma. Blood 2002;100:4629–39.
[11] Robichaud GA, Nardini M, Laflamme M, Cuperlovic-Culf M, Ouellette RJ. Human Pax-5 C-terminal isoforms possess distinct transactivation properties and are differentially modulated in normal and malignant B cells. J Biol Chem 2004;279:49956–63.
[12] Dorfler P, Busslinger M. C-terminal activating and inhibitory domains determine the transactivation potential of BSAP (Pax-5), Pax-2 and Pax-8. EMBO J 1996;15:1971–82.
[13] Nishihara M, Wada Y, Ogami K, Ebihara Y, Ishii T, Tsuji K, et al. A combination of stem cell factor and granulocyte colony-stimulating factor enhances the growth of human progenitor B cells supported by murine stromal cell line MS-5. Eur J Immunol 1998;28:855–64.
[14] Ohkawara JI, Ikebuchi K, Fujihara M, Sato N, Hirayama F, Yamaguchi M, et al. Culture system for extensive production of $CD19^+IgM^+$ cells by human cord blood $CD34^+$ progenitors. Leukemia 1998;12:764–71.
[15] Nakano T, Kodama H, Honjo T. Generation of lymphohematopoietic cells from embryonic stem cells in culture. Science 1994;265:1098–101.
[16] Tsuji T, Itoh K, Nishimura-Morita Y, Watanabe Y, Hirano D, Mori KJ, et al. $CD34^{high+}$ $CD38^{(low/-)}$ cells generated in a xenogenic co-culture system are capable of both long-term hematopoiesis and multiple differentiation. Leukemia 1999;13:1409–19.
[17] Yang AX, Mejido J, Luo Y, Zeng X, Schwartz C, Wu T, et al. Development of a focused microarray to assess human embryonic stem cell differentiation. Stem Cells Dev 2005;14:270–84.
[18] Kitamura T, Koshino Y, Shibata F, Oki T, Nakajima H, Nosaka T, et al. Retrovirus-mediated gene transfer and expression cloning: powerful tools in functional genomics. Exp Hematol 2003;31:1007–14.
[19] International Human Genome Sequencing Consortium. Finishing the euchromatic sequence of the human genome. Nature 2004;431:931–45.
[20] Kozmik Z, Kurzbauer R, Dorfler P, Busslinger M. Alternative splicing of Pax-8 gene transcripts is developmentally regulated and generates isoforms with different transactivation properties. Mol Cell Biol 1993;13:6024–35.
[21] Tavassoli K, Ruger W, Horst J. Alternative splicing in PAX2 generates a new reading frame and extended conserved coding region at the carboxy terminus. Hum Genet 1997;101:371–5.

ELSEVIER

EXPERIMENTAL HEMATOLOGY

Experimental Hematology 35 (2007) 407–415

Monitoring of disease progression by bioluminescence imaging and magnetic resonance imaging in an animal model of hematologic malignancy

Yusuke Inoue[a], Kiyoko Izawa[b], Arinobu Tojo[b], Yukihiro Nomura[c], Rieko Sekine[b], Naoki Oyaizu[d], and Kuni Ohtomo[c]

[a]*Department of Radiology, Institute of Medical Science;* [b]*Division of Molecular Therapy, Advanced Clinical Research Center, Institute of Medical Science;* [c]*Department of Radiology, Graduate School of Medicine;* [d]*Department of Laboratory Medicine, Institute of Medical Science, University of Tokyo, Tokyo, Japan*

(Received 7 July 2006; revised 13 November 2006; accepted 13 November 2006)

Objective. **We evaluated disease progression in a mouse model of a hematologic malignancy using a multimodality approach that included bioluminescence imaging (BLI) and magnetic resonance imaging (MRI). We aimed to examine the feasibility and capability of BLI and MRI and to establish techniques for quantitative assessment of disease severity.**

Methods. **Mice were inoculated intravenously with Ba/F3 cells transduced with firefly luciferase and p190 BCR-ABL genes. Disease progression in a given mouse was observed longitudinally by in vivo BLI and MRI (n = 5). Imaging studies, including in vivo BLI and MRI of living mice and ex vivo BLI of excised organs, were also performed at various time points (n = 4, 3, 4, and 4 at 1, 2, 3, and 4 weeks after cell inoculation).**

Results. **Longitudinal studies allowed the assessment of disease progression for each mouse, and an approximately 4-log increase in whole-body BLI signal was shown after initial detection. MRI demonstrated progressive hepatosplenomegaly and growth of hepatic nodules. Ex vivo BLI demonstrated proliferation of the implanted cells in various organs including bone marrow, and the signal for each organ increased with time (Spearman's rank correlation coefficient, R = 0.831–0.914) and as the whole-body signal, observed by in vivo BLI, increased (R = 0.921–0.982). MRI measurements of liver and spleen volumes were shown to have excellent accuracy and volume increases significantly correlated with the BLI organ signal (liver, R = 0.875; spleen, R = 0.971).**

Conclusion. **BLI and MRI allow repeated assessment of disease progression in a mouse model of a hematologic malignancy and provide quantitative markers of disease severity. BLI and MRI measurements reveal different details of disease progression and may play complementary roles in comprehensive assessment.** © **2007 International Society for Experimental Hematology. Published by Elsevier Inc.**

Noninvasive imaging is increasingly used to evaluate animal models of malignant neoplasms because it permits repeated assessment of disease progression and therapeutic effect in the same animal. In vivo bioluminescence imaging (BLI) is a promising technology for monitoring tumor model animals [1,2]. Typically, mice are inoculated with tumor cells stably expressing firefly luciferase and then injected with D-luciferin. Firefly luciferase catalyzes the oxidation of D-luciferin [3] while causing light emission. The resulting luminescence images are acquired using a charge-coupled device (CCD) camera and reflect the number and whole-body distribution of the implanted cells. In vivo BLI is noninvasive, convenient, and detects luciferase-expressing cells with high sensitivity. Another important advantage of the technique is that it allows quantitation of emitted light intensity and thus facilitates data analysis. In vivo BLI signals have been proven to reflect tumor burden in various models having subcutaneous [4–6], cerebral [7,8], hepatic [9,10], splenic [11], pulmonary [12], prostatic [13], or peritoneal lesions [14] and are accepted as quantitative indices of disease severity.

The application of in vivo BLI to animal models of hematologic malignancies has also been reported [15–18]. Systemic abnormalities occur in hematologic malignancies;

Offprint requests to: Yusuke Inoue, M.D., Department of Radiology, Institute of Medical Science, University of Tokyo, 4-6-1 Shirokanedai, Minato-ku, Tokyo 108-8639, Japan; E-mail: inoueys-tky@umin.ac.jp

0301-472X/07 $–see front matter.
doi: 10.1016/j.exphem.2006.11.006

in the model animals, various numbers of tumor cells are found in several organs, including bone marrow, lymph nodes, liver, and spleen. Because whole-body tumor burden is difficult to assess, survival is used as the primary endpoint. Survival assessment is time-consuming, however, and requires many animals to yield statistically relevant results. Furthermore, because survival can be influenced by factors other than tumor progression, accurate interpretation of the data can be obscured. The use of in vivo BLI signals as quantitative markers of disease severity may improve experimental efficiency. However, simultaneous presence of signals from various organs at various depths may impair the reliability of in vivo BLI quantitation in hematologic malignancies.

Luciferase-expressing organs can be determined easily by imaging the excised organs after D-luciferin injection using a CCD camera [12,19,20]. This procedure, called ex vivo BLI, enhances the detectability of luciferase expression [12,19] and provides a quantitative marker of luciferase expression in each organ [20]. Because luciferase-catalyzed oxidation of D-luciferin requires accessible oxygen, exposure to the atmosphere plays a critical role in ex vivo BLI, and bone destruction is required to demonstrate luciferase activity in the bone marrow after death [21]. An ex vivo imaging method for whole-body evaluation of bone marrow lesions has not yet been established.

Magnetic resonance imaging (MRI) can provide tomographic images containing detailed morphologic information. It permits visualization of internal organs, detection and localization of lesions, and measurement of organ and tumor size. Efforts to increase its convenience may enhance its popularity as a tool for small-animal research [22,23]. Animal models of hematologic malignancies often develop hepatosplenomegaly, and the sizes of the liver and spleen serve as markers of disease severity. MRI may aid in assessing progression of hematologic malignancies because it can be used to determine liver [24,25] and spleen [26] volumes.

In this study, we evaluated disease progression in a mouse model of hematologic malignancy using BLI and MRI. Our objective was to investigate the feasibility and potential of BLI and MRI evaluations of disease progression in hematologic malignancies and to establish techniques for quantitative assessment of disease severity.

Materials and methods

Cell lines

The interleukin-3 (IL-3)-dependent murine pro-B-cell line Ba/F3 was cotransfected with the firefly luciferase gene and the wild-type p190 BCR-ABL fusion gene using a retroviral method that was described previously [27], and the newly established cells were termed Ba/F3-Luc/Wt cells. The cDNA encoding firefly luciferase was excised from the pGL3-basic vector (Promega, Madison, WI, USA), and the long-term stability of luciferase expression in the established cells was confirmed in vitro. The p190 BCR-ABL gene is important in the development of acute lymphoblastic leukemia [28] and causes factor-independent, autonomous proliferation when transformed into Ba/F3 cells [29]. The Ba/F3-Luc/Wt cells were maintained in RPMI 1640 medium (Invitrogen, Grand Island, NY, USA) supplemented with 10% (v/v) fetal bovine serum (JRH Biosciences, Lenexa, KS, USA) and 1% penicillin/streptomycin (Invitrogen) in the absence of IL-3. Cell cultures were incubated at 37°C under 5% CO_2.

Animals

Eight-week-old female BALB/c nu/nu mice were inoculated with Ba/F3-Luc/Wt cells (2×10^6 cells, suspended in 0.1 mL phosphate-buffered saline) intravenously via the tail vein. The mice were obtained from SLC Japan (Tokyo, Japan) and were handled according to the guidelines of the Institute of Medical Science, University of Tokyo. The experiments were approved by the committee for animal research at the institution.

Longitudinal assessment in individual mice

We performed a longitudinal assessment of disease progression in five Ba/F3-Luc/Wt cell-inoculated mice using in vivo BLI and MRI. Both imaging studies were repeated 3 and 7 days after inoculation and then weekly until spontaneous death. To determine the baseline volumes of the liver and spleen, MRI was also performed 3 days before inoculation.

In vivo BLI was performed using a cooled CCD camera system (IVIS Imaging System 100; Xenogen, Alameda, CA, USA). The inoculated mice received an intraperitoneal injection of 150 mg/kg D-luciferin (Beetle Luciferin Potassium Salt, Promega) and were placed in the light-tight chamber of the CCD camera system under isoflurane anesthesia. Beginning 4 minutes after injection, photographic and luminescent images in the dorsal, left-lateral, ventral, and right-lateral projections were acquired. The data acquisition series of four projections was repeated three times; consequently, a single imaging session provided 12 luminescence images. The luminescence image represents light emission from the luciferase-expressing cells, and the photographic image is for the localization of the bioluminescent signal on the surface of the mouse. The exposure time for luminescence imaging varied from 1 to 60 seconds, depending on the intensity of luminescence.

After the completion of in vivo BLI, mice were injected subcutaneously with gadobenate dimeglumine (Gd-BOPTA, 0.1 mmol/kg), a hepatobiliary contrast agent for MRI [30]. MRI was performed on a compact MRI system (MRmini, MRTechnology, Tsukuba, Japan) using a 1-T permanent magnet and a solenoid coil of a 30-mm inner diameter [22,23]. Because the MRI system was small and caused only limited magnetic field leakage, the MRI and CCD camera systems were placed together without magnetic shielding in a $3 \times 8\text{-m}^2$ room in a specific pathogen-free animal facility. Under isoflurane anesthesia, mice were fixed in the prone position on a dedicated holder and inserted into the magnet bore. Three-dimensional, T1-weighted images of the entire trunk were obtained using a fast low-angle shot sequence in the coronal and sagittal planes. Data acquisition was started about 15 minutes after Gd-BOPTA injection. Scan parameters were as follows: repetition time, 40 ms; echo time, 3.6 and 6.7 ms; flip angle, 51°; in-plane matrix size, 256×128; slab partition, 64; number of excitation, 1; acquisition time, 5 minutes 28 seconds. Imaging with echo times of 3.6 and 6.7 ms provided opposed-phase and in-phase images,

respectively. The in-plane pixel size was 0.26 mm × 0.26 mm, and the slice thickness was 0.52 mm. Because a three-dimensional sequence was used, no gaps were present between slices.

Comparison of in vivo and postmortem findings

Mice were examined successively by in vivo BLI and MRI and ex vivo BLI at 1, 2, 3, and 4 weeks after cell inoculation (n = 4, 3, 4, and 4). MRI was also performed 3 days before cell inoculation to determine hepatic and splenic volumes at baseline.

First, mice were injected with 100 mg/kg D-luciferin, and two sets of in vivo BLI images in the four different projections were acquired, resulting in a collection of eight images. Then, Gd-BOPTA was administered and MRI was performed. The methods of in vivo BLI and MRI were the same as described above, except for the difference in the dose of D-luciferin and the number of BLI images acquired.

After completion of MRI, the mice were again injected intraperitoneally with 100 mg/kg D-luciferin, and ex vivo BLI was performed to assess tumor burden on individual organs. Twelve minutes after additional D-luciferin injection, the mice were sacrificed by cervical dislocation. The liver, spleen, gastrointestinal tract accompanied by mesentery, genital organs including ovary and uterus, kidney, lung, and heart were harvested and imaged using the CCD camera system. The organs were turned over after the first imaging and imaged again. After the internal organs and skin of the mouse were removed, ventral and dorsal images of the remaining body were obtained. When focal light sources were detected, their origins were determined visually and excised. The remaining body and the presumptive light sources were imaged together to confirm the location of the luciferase-expressing cells. This procedure aided the identification of lymph node involvement. Finally, the skeleton was cut with scissors at 31 predetermined sites (vertebrae, 15 sites; limbs, eight sites; thoracic cage, four sites; iliac bones, two sites; skull, one site; mandible, one site), and ventral and dorsal images were again acquired to assess bone marrow tumor burden.

Data analysis

On each in vivo BLI image, a region of interest (ROI) encompassing the entire mouse except the tail was placed, and the total signal in the ROI was quantified using Living Image software (version 2.50; Xenogen). The total signals of all images obtained in a single imaging session were averaged to determine the whole-body signal intensity, which was used as a marker of whole-body tumor burden. In the longitudinal assessment in individual mice, the day of spontaneous death was recorded, and the presumptive whole-body signal intensity at death was calculated by extrapolating from the final two data points monoexponentially.

The signal intensity of each organ was calculated from ex vivo BLI of excised organs. An ROI encompassing each organ was defined, and the total signals for the two views of that organ were averaged. The averaged signal intensity was used as a marker of organ tumor burden. In addition, an ROI encompassing the entire skeleton was defined on the images of the body remaining after removing the internal organs, and the signal derived from the bone marrow was defined as the difference in signals before and after bone cutting. The mean value calculated from the ventral and dorsal views was used as a marker of bone marrow tumor burden.

The volumes of the liver and spleen were determined using MRI. Coronal, opposed-phase images were used for the measurement of liver volume. The contour of the liver was traced manually on each slice in which the liver was visualized, and the liver volume was calculated by summing the products of liver areas measured on each slice and slice thickness. Spleen volume was determined similarly using coronal, in-phase images. The choice between in-phase and opposed-phase imaging was based on the clarity of the margin of the target organ. In the comparison of in vivo and postmortem findings, the volume increase for each mouse was calculated as the volume at sacrifice minus the baseline volume.

Relationships between two parameters were examined by the Spearman's rank correlation and were considered statistically significant for p values < 0.05.

Results

Longitudinal assessment in individual mice

Five mice were repeatedly examined by in vivo BLI and MRI after inoculation with Ba/F3-Luc/Wt cells. In vivo BLI revealed foci indicative of tumor cell proliferation in four of the five mice at 3 days and in all mice at 1 week. Serial BLI studies showed that the intensity and extent of light emission gradually increased, indicating progression of the disease in various regions, including the head and neck, chest, abdomen, and limbs (Fig. 1). Involvement of the bone marrow, liver, and spleen was presumed, and splenic involvement could be determined confidently when a bright, splenic-shaped area was observed. However, the extensive distribution of light signals generally prevented confident identification of the involved organs.

Serial quantitative evaluation of light intensity for each mouse demonstrated that whole-body tumor burden increased with time after inoculation (Fig. 2A). Whole-body signal intensities ranged from 2.76×10^5 to 4.20×10^5 photons/s at 3 days in the four mice showing luminescent foci. Thereafter, an approximately 4-log increase in whole-body signal was demonstrated. Mice died spontaneously 30 to 71 days after inoculation. Although the rate of increase in light intensity was variable among mice, the presumptive signal intensity at death was relatively constant, in the range 5.24×10^9 to 1.98×10^{10} photons/s.

MRI obtained after the subcutaneous injection of a hepatobiliary contrast agent Gd-BOPTA demonstrated no evidence of proliferation of inoculated cells until 3 weeks after inoculation. Development and exacerbation of hepatosplenomegaly was observed beginning at 3 or 4 weeks, and the temporal profile of hepatosplenomegaly was variable among mice (Fig. 2B, C). In one mouse, definite splenomegaly was observed at 6 and 7 weeks, and it regressed spontaneously at 8 weeks. Because no substantial BLI signal was detected at the corresponding site, the transient splenomegaly was ascribed to enlargement and subsequent resolution of some nontumorous component.

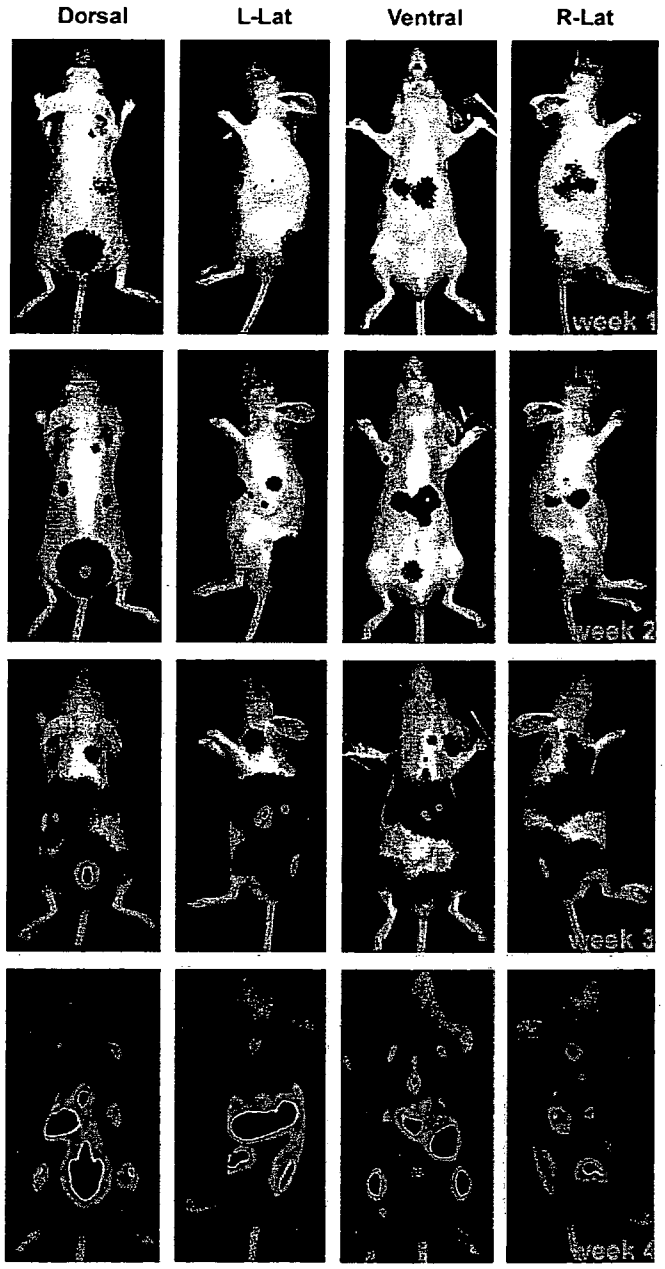

Figure 1. In vivo BLI of a mouse. The dorsal, left-lateral (L-Lat), ventral, and right-lateral (R-Lat) images obtained 1, 2, 3, and 4 weeks after cell inoculation are presented. The pseudocolor luminescent image (blue, green, yellow, and red from least to most intense) is overlaid on the grayscale photographic image. The same color scale was used for the images obtained at 2, 3, and 4 weeks, but the lower limit of the scale was decreased for the images obtained at 1 week because of their weak signals. Gradual proliferation of the inoculated cells in various regions is indicated. This mouse died on day 36.

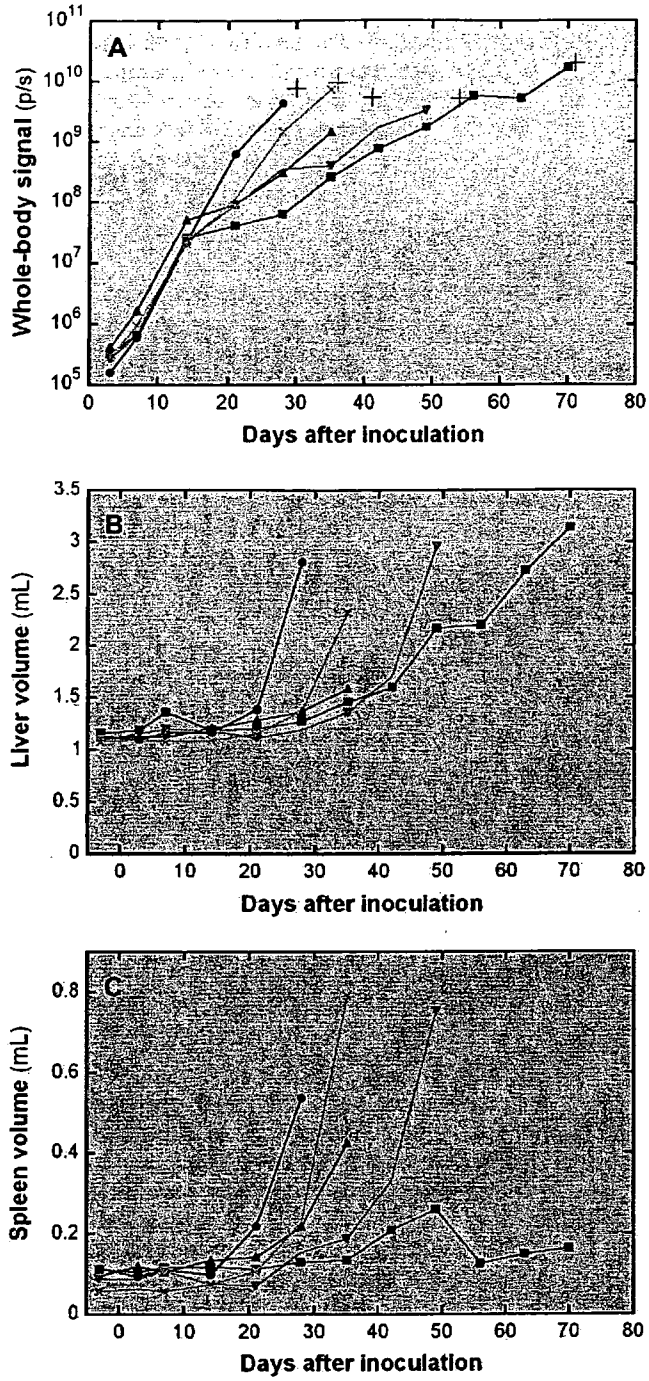

Figure 2. Time courses of BLI and MRI measurements in each mouse studied longitudinally: **(A)**, whole-body BLI signal; **(B)**, liver volume calculated from MRI; **(C)**, spleen volume calculated from MRI. The plus sign in panel **A** represents the day of spontaneous death and the presumptive signal intensity at death.

Hypointense hepatic nodules suggestive of nodular growth of the implanted cells were found in all mice at 3 weeks and gradually increased in size and number (Fig. 3). One mouse exhibited an enlarged ovary, and two mice exhibited enlarged para-aortic lymph nodes. Bone marrow abnormalities were not detected by MRI.

Comparison of in vivo and postmortem findings

To investigate the time course of disease progression in detail and to evaluate the utility of BLI and MRI in assessing disease severity, imaging studies consisting of in vivo BLI, MRI, and ex vivo BLI were performed 1, 2, 3, or 4 weeks after tumor cell inoculation (n = 4, 3, 4, 4). In vivo BLI

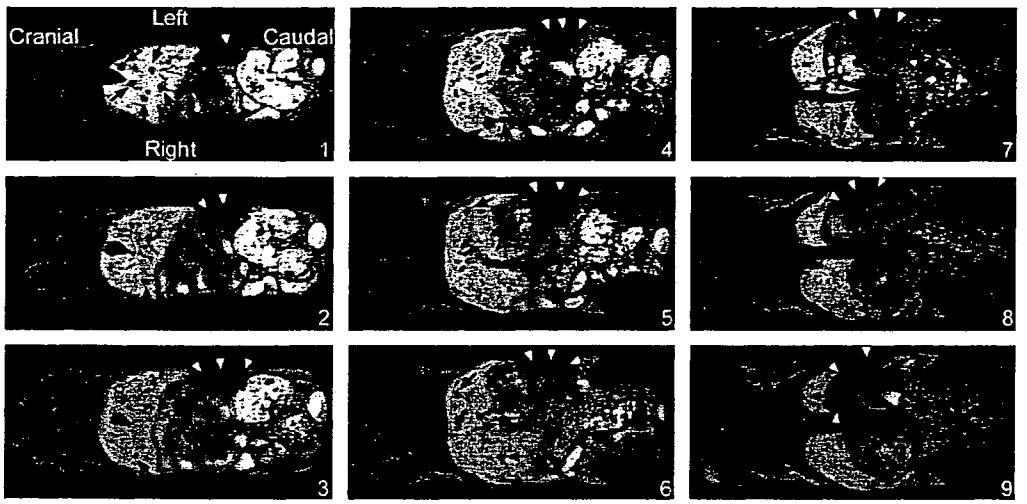

Figure 3. MRI of the trunk of the mouse presented in Figure 1, obtained 4 weeks after cell inoculation. The image number is given in the right lower corner of each panel, and image 1 is the most ventral image among those displayed in this figure. Normal hepatic parenchyma appears hyperintense (bright) due to the effect of the hepatobiliary contrast agent. Tiny, round, hypointense (dark) areas suggesting nodular growth of the inoculated cells are visible in addition to branched hypointense areas corresponding to intrahepatic vessels. Arrows indicate some of the nodules. Enlarged spleen appears as dark areas (white arrowheads).

again showed extensive light emission. Although identification of involved organs using in vivo BLI was difficult, ex vivo BLI of the excised organs clearly demonstrated substantial light emission from the liver, spleen, genital organs, lung, and gastrointestinal tract. Many nodular sources contributed to light signals in liver. Para-aortic lymph node involvement was shown in one and three mice at 3 and 4 weeks, respectively, and submandibular lymph node involvement was revealed in one mouse at 4 weeks. Bone cutting induced light emission from multiple sites, indicating bone marrow involvement (Fig. 4).

Whole-body signal intensity, as measured by in vivo BLI, increased significantly with time after inoculation (Fig. 5), and Spearman's rank correlation coefficient (R) was calculated to be 0.895 ($p < 0.001$). Organ signals, including bone marrow signal, also increased significantly with time (Fig. 5, Table 1). The whole-body signal correlated closely with the organ signals (Table 1).

The wet weights of the liver and spleen increased significantly with time after cell inoculation (liver, $R = 0.717$, $p < 0.01$; spleen, $R = 0.859$, $p < 0.01$). Progressive hepatosplenomegaly was also evident on MRI (liver, $R = 0.807$, $p < 0.01$; spleen, $R = 0.859$, $p < 0.01$), and the volumes of the liver and spleen, as measured by MRI, exhibited high correlations with their weights (Fig. 6). The increases in liver and spleen volume significantly correlated with their luminescence signals as detected by ex vivo BLI (Fig. 7).

Visual evaluation of MRI revealed no obvious abnormalities at 1 or 2 weeks after cell inoculation. Multiple hypointense liver nodules were noted in three and four mice at 3 and 4 weeks, respectively. Gross inspection of the excised liver revealed nodular lesions in these mice, and in livers of two of these mice, nodular growth of the implanted cells was confirmed by histopathologic examination (Fig. 8). Enlargement of para-aortic lymph nodes was evident on MRI in three mice at 4 weeks. Enlargement of the ovary was demonstrated in one mouse each at 3 and 4 weeks. Bone marrow lesions were not evident on MRI.

Discussion

In the present study, in vivo BLI revealed a gradual increase in the intensity and extent of light emission in mice over

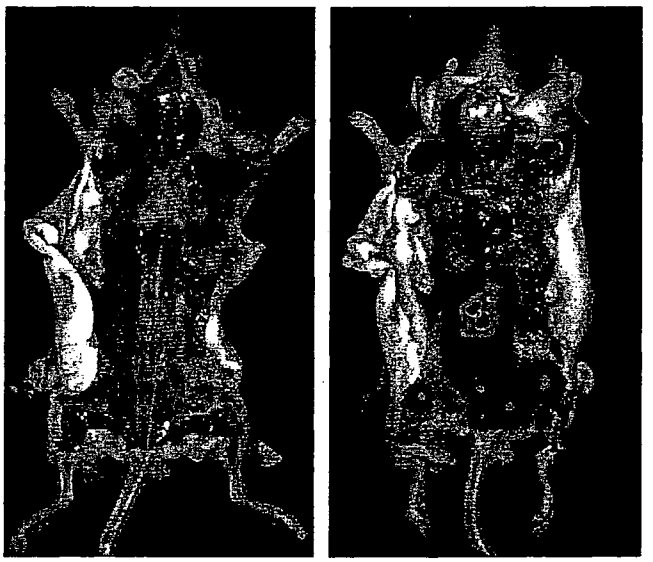

Figure 4. Ex vivo BLI of the mouse body remaining after removal of the internal organs. The dorsal images before (left) and after (right) bone cutting are presented using the same color scale. After bone cutting, bone marrow signals are indicated in the upper and lower limbs, skull, ribs, vertebrae, and pelvis.

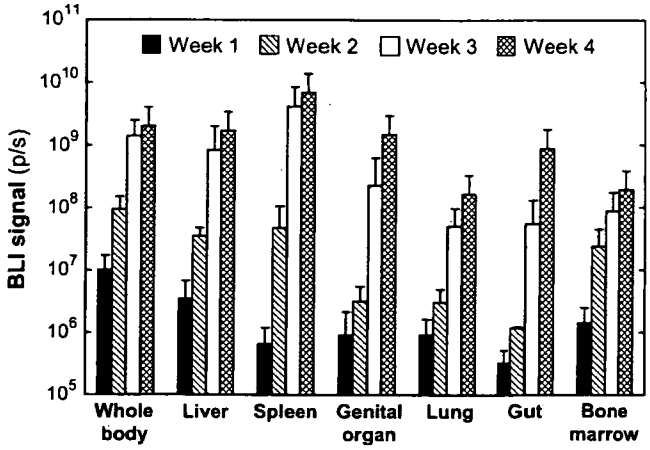

Figure 5. Whole-body and organ BLI signals determined 1, 2, 3, and 4 weeks after cell inoculation. Progressive increases are demonstrated for whole-body signals obtained by in vivo BLI and for organ signals obtained by ex vivo BLI. Note that additional D-luciferin injection was made before ex vivo BLI and that the total injection dose was different between in vivo and ex vivo BLI.

time after inoculation with model cells of a hematologic malignancy, and it yielded overviews of cell proliferation in various regions. However, definitive identification of the involved organs was difficult using the in vivo images; this problem appeared to be attributable to lack of detailed anatomic markers, low spatial resolution, projectional imaging, and multiple organ involvement. The bone marrow signal in particular can distribute extensively over internal organs, preventing reliable localization. Using ex vivo BLI, we observed cell proliferation in multiple organs beginning at the early stages of disease progression. Ex vivo BLI provides a detailed description of the organ distribution of the implanted cells. Interpretation of in vivo BLI results would be aided by prior knowledge of the cell distribution in a given model.

Table 1. Correlation of organ luminescence with time and whole-body luminescence

	Spearman's rank correlation coefficient	
Organ	Time	Whole-body signal
Liver	0.910*	0.982*
Spleen	0.895*	0.975*
Genital organ	0.831†	0.921*
Lung	0.844†	0.954*
Gut	0.910*	0.975*
Bone marrow	0.914*	0.939*

Values are Spearman's rank correlation coefficients between the signals of each organ (liver, spleen, genital organ, lung, gut, and bone marrow) and time after cell inoculation or whole-body signal.
*$p < 0.001$.
†$p < 0.01$.

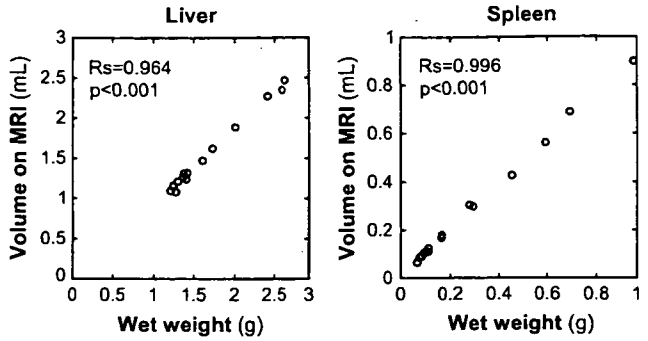

Figure 6. Relationship between organ wet weight and the organ volume determined by MRI. Excellent correlation is evident for the liver and spleen.

Although quantitative evaluation of disease severity is regarded as a major role of BLI, the presence of light signals from different depths and different organs may cause problems in systemic disease. The intensity of in vivo BLI signal strongly depends on the depth of the light source due to strong attenuation by overlying tissues [31,32]. To minimize the dependence of the data on the locations of luminescent foci, quantitative indices were calculated from images in four different projections. Multiple series of images from the four directions were acquired to reduce the influence of the positioning of the mouse. Temporal patterns of luminescence after D-luciferin injection can differ between different luciferase-bearing tissues [33,34], and multiple imaging is also expected to compensate for variations in the time course of luminescence among organs and among experiments. Because separation of the signals from different organs in vivo was difficult, ROIs encompassing the whole body were used.

The whole-body signal intensity calculated from in vivo BLI increased with time after cell inoculation and with the ex vivo BLI signals from the individual organs. Although the number of mice examined was relatively low,

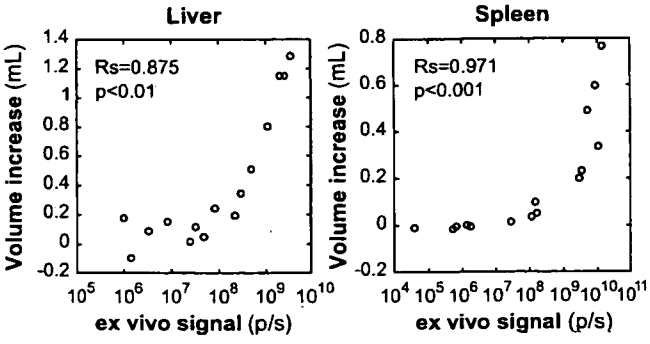

Figure 7. Relationship between ex vivo BLI organ signals and the organ volume increases determined by MRI. Intensification of the BLI signals of the liver (left) and spleen (right) correlates with enlargement of these organs.

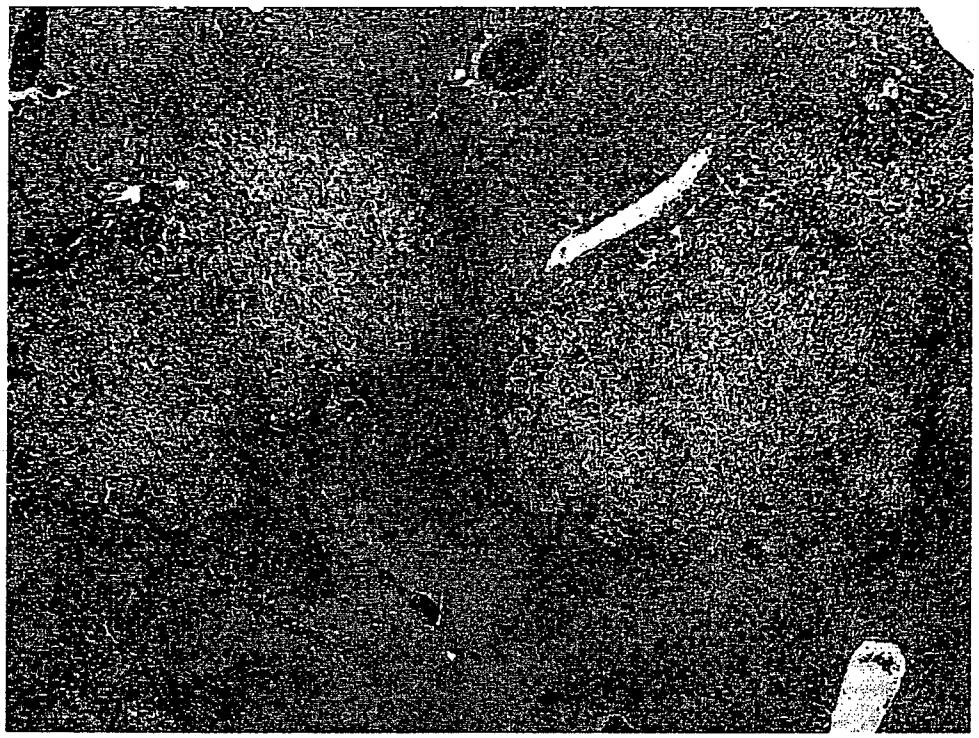

Figure 8. Histologic picture of the liver specimen sampled 4 weeks after cell inoculation. Nodular growth of the implanted cells is demonstrated. (Hematoxylin-eosin stain; original magnification, ×4.)

longitudinal imaging showed that the presumptive signal intensity at death was relatively constant despite large variations in the rate of signal increase, supporting use of the whole-body signal to represent disease severity. We were able to observe a 4-log signal increase between initial detection of luminescent foci and death, suggesting that in vivo BLI is suitable for use in early detection. It appears to allow quantitative and sensitive evaluation of whole-body disease progression in hematologic malignancies and may provide a useful surrogate marker for survival. High-throughput screening using BLI may facilitate selection of candidates for further, more laborious evaluations of proposed novel treatment strategies.

Bone marrow luminescence after death requires destruction of the bone [21]. In the present study, the skeleton was cut at many sites to assess the systemic distribution of the implanted cells in the bone marrow. Bone cutting generated many luminescent foci, indicating cell proliferation in the marrow. The bone marrow signal intensity was calculated as the difference in signals before and after bone cutting, and it increased with time after inoculation and with whole-body signal intensity. These observations suggest that this method is appropriate for determination of the distribution and number of implanted cells in the bone marrow. Whole-body assessment of cell proliferation in the bone marrow is a challenging task, and this technique should be useful in blood cell transplantation experiments as well as in studies of hematologic malignancies. Some areas were presumed to have implanted cells in the bone marrow, based on in vivo imaging, but did not emit light after bone cutting. In this case, the luminescent cells may have been located at a site distant from the cut, so that their exposure to the atmosphere was insufficient for the luminescence reaction. Targeting the presumed light source in cutting would contribute to proving a luminescent focus to be of bone marrow origin.

Excellent accuracy of MRI volume measurements of the liver and spleen was elucidated. The spleen is recognized easily as the hypointense areas in T1-weighted images. The liver, on the other hand, has an intensity similar to that of the adjacent soft tissues in T1-weighted images unless a contrast agent is injected. The lower border of the liver may be unclear, impairing the reliability of volume measurement. Although an extracellular contrast agent for liver volumetry has been used in order to improve the accuracy of MRI liver volumetry [24,25], the distribution of an extracellular agent is nonspecific and does not necessarily facilitate recognition of the liver border [25]. In contrast to extracellular agents, Gd-BOPTA elevates the signal intensity of normal liver parenchyma in T1-weighted images through its selective uptake by functioning hepatocytes, leading to better visualization of the liver and enhanced contrast between the liver and intrahepatic tumors [35,36]. The use of Gd-BOPTA, as well as the acquisition of thin, contiguous slices, appears to have contributed to the successful results of the present study.

MRI allowed longitudinal, quantitative assessment of hepatosplenomegaly. The volumes measured by MRI increased with time after inoculation, and these volume increases correlated with their respective organ signals in ex vivo BLI. MRI measurements of hepatic and splenic volumes appear to offer a potent tool for the assessment of the severity of hematologic malignancies. MRI also revealed lymph node and ovary enlargement and the appearance and growth of intrahepatic nodules. Bone marrow lesions were not evident on MRI. In human clinical MRI, bone marrow involvement is characterized by a focal increase in water content accompanied by a decrease in fat content. The high proportion of water in normal marrow may disturb the detection of bone marrow involvement in young mice. The use of T2-weighted imaging sequence or contrast agents may aid MRI evaluation of bone marrow involvement [37].

Although both the in vivo BLI and MRI techniques permitted longitudinal assessment in a mouse model of hematologic malignancy, in vivo BLI was able to demonstrate cell proliferation at an earlier time point than MRI; the higher sensitivity of BLI may be attributable to its high specificity for luciferase-expressing cells. In monitoring of tumors using in vivo BLI, possible discrepancies between light intensity and cell number are a matter of some concern [27]. Validation of the BLI signal as a marker of disease severity for each experimental model would be desirable. Furthermore, the requirement for stable luciferase expression may hinder use of BLI monitoring. Morphologic assessment by MRI does not require genetic manipulation, and the resulting information about organ location and shape and the presence and position of lesions in each mouse should aid the interpretation of in vivo BLI results, especially when normal anatomy is distorted (e.g., due to hepatosplenomegaly). Possible discrepancies between the extent of morphologic change measured by MRI and proliferation of implanted cells should be noted. In our longitudinal study, we observed transient splenomegaly due to an increase in nontumorous components. BLI may be useful in determining whether morphologic changes observed using MRI are a direct result of implanted cell proliferation or an indirect result, due to secondary reaction(s). In addition, combined interpretation of BLI and MRI may facilitate detection of MRI abnormalities. Both BLI and MRI are useful tools for the evaluation of disease progression in mouse models of hematologic malignancies, and multimodality imaging is expected to offer further benefits.

In conclusion, BLI and MRI allow repeated, quantitative evaluation of systemic disease induced by intravenous inoculation of luciferase-expressing model cells of a hematologic malignancy. Whole-body tumor burden as determined using in vivo BLI may serve as a sensitive, quantitative surrogate marker of systemic disease severity. MRI allows accurate measurement of hepatic and splenic volumes and, therefore, evaluation of disease progression, with no need for additional genetic manipulation. BLI and MRI may play complementary roles, and a multimodality approach using BLI and MRI may be useful for comprehensive assessment of hematologic malignancies.

Acknowledgments

This work was supported in part by Grants-in-Aid for Scientific Research from the Ministry of Education, Culture, Sports, Science and Technology of Japan.

References

1. Contag CH, Jenkins D, Contag PR, Negrin RS. Use of reporter genes for optical measurements of neoplastic disease in vivo. Neoplasia. 2000;2:41–52.
2. Edinger M, Cao YA, Hornig YS, et al. Advancing animal models of neoplasia through in vivo bioluminescence imaging. Eur J Cancer. 2002;38:2128–2136.
3. Day JC, Tisi LC, Bailey MJ. Evolution of beetle bioluminescence: the origin of beetle luciferin. Luminescence. 2004;19:8–20.
4. Choy G, O'Connor S, Diehn FE, et al. Comparison of noninvasive fluorescent and bioluminescent small animal optical imaging. Biotechniques. 2003;35:1022–1030.
5. Paroo Z, Bollinger RA, Braasch DA, et al. Validating bioluminescence imaging as a high-throughput, quantitative modality for assessing tumor burden. Mol Imaging. 2004;3:117–124.
6. Nogawa M, Yuasa T, Kimura S, et al. Monitoring luciferase-labeled cancer cell growth and metastasis in different in vivo models. Cancer Lett. 2005;217:243–253.
7. Rehemtulla A, Stegman LD, Cardozo SJ, et al. Rapid and quantitative assessment of cancer treatment response using in vivo bioluminescence imaging. Neoplasia. 2000;2:491–495.
8. Szentirmai O, Baker CH, Lin N, et al. Noninvasive bioluminescence imaging of luciferase expressing intracranial U87 xenografts: correlation with magnetic resonance imaging determined tumor volume and longitudinal use in assessing tumor growth and antiangiogenic treatment effect. Neurosurgery. 2006;58:365–372.
9. Nyati MK, Symon Z, Kievit E, et al. The potential of 5-fluorocytosine/cytosine deaminase enzyme prodrug gene therapy in an intrahepatic colon cancer model. Gene Ther. 2002;9:844–849.
10. Smakman N, Martens A, Kranenburg O, Borel Rinkes IH. Validation of bioluminescence imaging of colorectal liver metastases in the mouse. J Surg Res. 2004;122:225–230.
11. Mandl SJ, Mari C, Edinger M, et al. Multi-modality imaging identifies key times for annexin V imaging as an early predictor of therapeutic outcome. Mol Imaging. 2004;3:1–8.
12. Jenkins DE, Oei Y, Hornig YS, et al. Bioluminescent imaging (BLI) to improve and refine traditional murine models of tumor growth and metastasis. Clin Exp Metastasis. 2003;20:733–744.
13. Scatena CD, Hepner MA, Oei YA, et al. Imaging of bioluminescent LNCaP-luc-M6 tumors: a new animal model for the study of metastatic human prostate cancer. Prostate. 2004;59:292–303.
14. Zeamari S, Rumping G, Floot B, Lyons S, Stewart FA. In vivo bioluminescence imaging of locally disseminated colon carcinoma in rats. Br J Cancer. 2004;90:1259–1264.
15. Edinger M, Cao YA, Verneris MR, Bachmann MH, Contag CH, Negrin RS. Revealing lymphoma growth and the efficacy of immune cell therapies using in vivo bioluminescence imaging. Blood. 2003; 101:640–648.

16. Shah NP, Tran C, Lee FY, Chen P, Norris D, Sawyers CL. Overriding imatinib resistance with a novel ABL kinase inhibitor. Science. 2004; 305:399–401.
17. Wu KD, Cho YS, Katz J, et al. Investigation of antitumor effects of synthetic epothilone analogs in human myeloma models in vitro and in vivo. Proc Natl Acad Sci U S A. 2005;102:10640–10645.
18. Weisberg E, Manley PW, Breitenstein W, et al. Characterization of AMN107, a selective inhibitor of native and mutant Bcr-Abl. Cancer Cell. 2005;7:129–141.
19. Yoshimitsu M, Sato T, Tao K, et al. Bioluminescent imaging of a marking transgene and correction of Fabry mice by neonatal injection of recombinant lentiviral vectors. Proc Natl Acad Sci U S A. 2004; 101:16909–16914.
20. Carlsen H, Moskaug JO, Fromm SH, Blomhoff R. In vivo imaging of NF-kappa B activity. J Immunol. 2002;168:1441–1446.
21. Inoue Y, Izawa K, Tojo A, Sekine R, Okubo T, Ohtomo K. Light emission requires exposure to the atmosphere in ex vivo bioluminescence imaging. Mol Imaging. 2006;5:53–56.
22. Haishi T, Uematsu T, Matsuda Y, Kose K. Development of a 1.0 T MR microscope using a Nd-Fe-B permanent magnet. Magn Reson Imaging. 2001;19:875–880.
23. Inoue Y, Nomura Y, Haishi T, et al. Imaging of living mice using a 1-T compact magnetic resonance imaging system. J Magn Reson Imaging. 2006;24:901–907.
24. Garbow JR, Kataoka M, Flye MW. MRI measurement of liver regeneration in mice following partial hepatectomy. Magn Reson Med. 2004; 52:177–180.
25. Inderbitzin D, Gass M, Beldi G, et al. Magnetic resonance imaging provides accurate and precise volume determination of the regenerating mouse liver. J Gastrointest Surg. 2004;8:806–811.
26. Allegrini PR, Wachsmuth ED. Course of murine leukemia retrovirus infection determined in vivo by magnetic resonance imaging. Lab Invest. 1990;63:568–575.
27. Inoue Y, Tojo A, Sekine R, et al. In vitro validation of bioluminescent monitoring of disease progression and therapeutic response in leukaemia model animals. Eur J Nucl Med Mol Imaging. 2006;33: 557–565.
28. Copelan EA, McGuire EA. The biology and treatment of acute lymphoblastic leukemia in adults. Blood. 1995;85:1151–1168.
29. Li S, Ilaria RL Jr, Million RP, Daley GQ, Van Etten RA. The P190, P210, and P230 forms of the BCR/ABL oncogene induce a similar chronic myeloid leukemia-like syndrome in mice but have different lymphoid leukemogenic activity. J Exp Med. 1999;189:1399–1412.
30. Reimer P, Schneider G, Schima W. Hepatobiliary contrast agents for contrast-enhanced MRI of the liver: properties, clinical development and applications. Eur Radiol. 2004;14:559–578.
31. Rice BW, Cable MD, Nelson MB. In vivo imaging of light-emitting probes. J Biomed Opt. 2001;6:432–440.
32. El Hilali N, Rubio N, Martinez-Villacampa M, Blanco J. Combined noninvasive imaging and luminometric quantification of luciferase-labeled human prostate tumors and metastases. Lab Invest. 2002;82: 1563–1571.
33. Honigman A, Zeira E, Ohana P, et al. Imaging transgene expression in live animals. Mol Ther. 2001;4:239–249.
34. Burgos JS, Rosol M, Moats RA, et al. Time course of bioluminescent signal in orthotopic and heterotopic brain tumors in nude mice. Biotechniques. 2003;34:1184–1188.
35. Kreft BP, Tanimoto A, Stark DD, et al. Enhancement of tumor-liver contrast-to-noise ratio with gadobenate dimeglumine in MR imaging of rats. J Magn Reson Imaging. 1993;3:41–49.
36. Kim YK, Lee JM, Kim CS. Gadobenate dimeglumine-enhanced liver MR imaging: value of dynamic and delayed imaging for the characterization and detection of focal liver lesions. Eur Radiol. 2004;14:5–13.
37. Gauvain KM, Garbow JR, Song SK, Hirbe AC, Weilbaecher K. MRI detection of early bone metastases in b16 mouse melanoma models. Clin Exp Metastasis. 2005;22:403–411.

Eur J Nucl Med Mol Imaging (2007) 34:2048–2056
DOI 10.1007/s00259-007-0583-2

ORIGINAL ARTICLE

In vivo fluorescence imaging of the reticuloendothelial system using quantum dots in combination with bioluminescent tumour monitoring

Yusuke Inoue · Kiyoko Izawa · Kohki Yoshikawa · Haruyasu Yamada · Arinobu Tojo · Kuni Ohtomo

Received: 9 April 2007 / Accepted: 14 August 2007 / Published online: 21 September 2007

Abstract
Purpose We characterised in vivo fluorescence imaging (FLI) of the reticuloendothelial system using quantum dots (QD) and investigated its use in combination with in vivo bioluminescence imaging (BLI).
Materials and methods In vivo FLI was performed in five mice repeatedly after the intravenous administration of QD without conjugation to targeting ligands. Ex vivo FLI of the excised organs was performed 24 h after QD injection in three mice. Seven days after intravenous inoculation of luciferase-expressing model cells of a haematological malignancy, mice were injected with the QD or saline (n=5 each), and combined BLI/FLI was performed repeatedly. Additional five mice inoculated with the tumour cells were examined by in vivo BLI/FLI, and the structures harbouring bioluminescent foci were determined by ex vivo BLI. The utility of combining FLI with bioluminescent tumour monitoring was evaluated.
Results In vivo FLI after QD injection allowed long-term, repeated observation of the reticuloendothelial system in individual mice, although fluorescence intensity and image contrast gradually decreased over time. Ex vivo FLI verified selective accumulation in reticuloendothelial structures. The administration of QD did not affect whole-body bioluminescent signal intensities during longitudinal tumour monitoring. In vivo BLI/FLI, accompanied by fusion of both images, improved the accuracy and confidence level of the localisation of the bioluminescent foci.
Conclusions In vivo FLI using QD provides an overview of the reticuloendothelial system in living mice. In combination with bioluminescent tumour monitoring, fluorescent reticuloendothelial imaging is expected to provide valuable information for lesion localisation.

Keywords Quantum dots · Fluorescence imaging · Bioluminescence imaging · Luciferase · Image fusion

Y. Inoue (✉) · H. Yamada
Department of Radiology, Institute of Medical Science,
University of Tokyo,
4-6-1 Shirokanedai, Minato-ku,
Tokyo 108-8639, Japan
e-mail: inoueys-tky@umin.ac.jp

K. Izawa · A. Tojo
Division of Molecular Therapy,
Advanced Clinical Research Centre,
Institute of Medical Science,
University of Tokyo,
Tokyo, Japan

K. Yoshikawa
Department of Radiotechnical Sciences,
Faculty of Radiological Health Sciences,
Komazawa University,
Tokyo, Japan

K. Ohtomo
Department of Radiology, Graduate School of Medicine,
University of Tokyo,
Tokyo, Japan

Introduction

The role of in vivo imaging in small animal experiments is expanding. Imaging technologies permit repeated assessment of individual animals to evaluate disease progression, therapeutic efficacy and pharmacokinetics. Each animal can be used as its own control, leading to greater reliability of the results even when a small number of animals are used. Imaging modalities applied in small animal studies include magnetic resonance imaging (MRI), computed tomography (CT), single photon emission computed tomography

supplied by Xenogen. Although QD absorption is more efficient at shorter wavelengths, we chose excitation light just below the emission band to reduce attenuation in tissues [19]. The field-of-view (FOV) was set at 15 cm for BLI/FLI and 20 cm for FLI alone because uniformity of excitation is better for a larger FOV and we were seeking to quantify fluorescent signals in the experiments of FLI alone. Other imaging parameters were adjusted mainly depending on the intensity of fluorescent signals. An exposure time of 1 to 8 s and binning of 2 or 4 were used. For BLI, we acquired photographic and bioluminescent images. Bioluminescent images were taken with an exposure time of 1 to 60 s, binning of 4 or 8 and an FOV of 15 cm. Quantitative analysis of signal intensity was performed using Living Image software (version 2.50; Xenogen).

Serial in vivo FLI

We evaluated the visualisation of the reticuloendothelial system longitudinally by in vivo FLI of living mice after systemic administration of QD. Qdot 705 ITK amino (PEG) quantum dots (amino-PEG–QD; Invitrogen) were used without conjugation to targeting ligands. Five mice were injected with 5 pmol/g amino-PEG–QD (5 ul/g) intravenously via the tail vein. For each mouse, FLI was performed before injection and 1, 3, 6 and 24 h after injection, followed by imaging at 3, 7, 14, 21 and 28 days post-injection. FLI images in the ventral, right-lateral, dorsal and left-lateral projections were acquired at each time point. Structures delineated on the images were evaluated visually using various display conditions that were optimised for observing each structure. To assess the temporal pattern of amino-PEG–QD uptake quantitatively, a region-of-interest (ROI) was defined for the liver, spleen, spine and inguinal lymph nodes, and the mean signal intensity for each structure was determined. ROI of the same size were used for a given structure and were positioned in the brightest area of the structure. ROI for the liver, spleen and spine were set on the ventral, left-lateral and dorsal images, respectively. ROI for the right and left inguinal lymph nodes were placed on the right-lateral and left-lateral images, respectively, and the signal intensity in the two ROI was averaged to determine the signal intensity of the inguinal lymph node.

Ex vivo FLI

We performed ex vivo FLI of the excised organs to evaluate the distribution of amino-PEG–QD. Three mice were injected intravenously with 5 pmol/g amino-PEG–QD, and in vivo FLI images in the four projections were acquired 24 h later. Subsequently, mice were killed by cervical dislocation. Skin and peritoneum on the ventral side were removed and a ventral FLI image was collected. Superficial lymph nodes presumably corresponding to focal signals on the image were excised and imaged together with the remaining body to confirm lymph node uptake. Then, the liver, spleen, gastrointestinal tract, ovary and uterus, kidney, adrenal glands, lung and heart were harvested and imaged. The remaining body was imaged after removal of the anterior thoracic wall, and deep lymph node uptake was assessed in a similar manner to superficial node assessment. The body was imaged in the dorsal projection after removing the skin. Finally, the brain and femoral muscle were harvested and imaged. Three control mice without amino-PEG–QD administration were examined similarly. The signal intensity of each organ was determined by placing the ROI on the FLI images of the excised organs. For the spine, an ROI was set on the dorsal image obtained after skin removal.

Longitudinal in vivo BLI/FLI

We injected amino-PEG–QD into mice inoculated with luciferase-expressing cells and performed in vivo BLI/FLI repeatedly to determine the feasibility of the combined imaging and to evaluate the effect of amino-PEG–QD on the quantitative results of bioluminescent tumour monitoring. Ten mice were inoculated with Ba/F3–Luc/Wt cells (1×10^6 cells, suspended in 0.1 ml phosphate-buffered saline) intravenously via the tail vein. Before cell inoculation and 5 days post-inoculation, in vivo BLI was performed and whole-body signal intensity was measured. Mice were divided into two groups, the QD group and the control group, which had a comparable whole-body signal 5 days post-inoculation. Seven days after cell inoculation, mice in the QD group were injected with 5 pmol/g amino-PEG–QD intravenously, and in vivo BLI/FLI was performed about 3 h later. For BLI/FLI, mice were given an intraperitoneal injection of 150 mg/kg D-luciferin (beetle luciferin potassium salt; Promega) and a ventral BLI image was acquired 6 min later. Immediately after the completion of the acquisition, a ventral FLI image was collected whilst the position of the mouse remained unchanged. Subsequently, BLI and FLI images were obtained in the right-lateral, dorsal and left-lateral projections. Additional BLI acquisition was performed in the four projections to reduce erroneous variations in bioluminescent signal intensity [14]. Control mice were intravenously injected with saline, instead of amino-PEG–QD, and two sets of BLI images in the four projections were acquired. Image acquisition was repeated 14, 21 and 28 days after cell inoculation (7, 14 and 21 days after QD or saline injection) without additional QD or saline injection.

On each BLI image, an ROI encompassing the entire mouse except the tail and distal ends of the limbs was defined, and the total signal in the ROI was measured. The total signals of all bioluminescent images obtained in a single imaging session were averaged to determine the whole-body signal intensity as a marker of whole-body tumour burden. For detailed comparison between BLI and FLI, fusion images were produced using general-purpose software (Adobe Photoshop 6.0; Adobe Systems, San Jose, CA) by overlaying the transparent, pseudo-colour bioluminescent image onto the grey-scale fluorescent image.

BLI/FLI assessment of lesion locations

We determined the locations of bioluminescent foci in mice inoculated with the luciferase-expressing cells using in vivo BLI/FLI, and evaluated the utility of combining FLI with bioluminescent tumour monitoring. Five mice were inoculated with 1×10^6 Ba/F3–Luc/Wt cells intravenously. Imaging studies were performed in three and two mice, 7 and 9 days post-inoculation, respectively. On the day of imaging, mice were injected intravenously with 5 pmol/g amino-PEG–QD, and in vivo BLI/FLI was performed 1–3 h later. A single set of BLI and FLI images was acquired in each of the four projections after intraperitoneal injection of 150 mg/kg D-luciferin.

Following the completion of in vivo BLI/FLI, about ten representative bioluminescent foci were selected for each mouse, and the structures harbouring the foci were determined by ex vivo BLI [14, 20, 21]. Bioluminescent foci located in the head and the peripheral portions of the limbs were excluded because lesions in these locations are not generally problematic. After the mice were killed by cervical dislocation, the skin and peritoneum on the ventral side were removed, and a ventral BLI image was collected. If necessary, additional images were obtained after exposing the areas presumably bearing the foci. For example, when a light source was presumed to be at the right-lateral portion of the liver and was not observed on the ventral image, the right side of the liver was exposed and turned towards the camera. Thereafter, the liver, spleen, gastrointestinal tract, ovary and uterus, kidney, adrenal glands, lung and heart were harvested, and BLI images were acquired. Following the removal of the internal organs and skin, the remaining body was imaged in the ventral and dorsal projections. Because bone destruction is required to demonstrate luciferase activity within the bone after death [22], the skeleton was cut with scissors at many positions and then BLI images to identify the bones containing luciferase-expressing cells were obtained.

The structures harbouring the representative bioluminescent foci were also determined visually by two radiologists independently. In the model animals, inoculated cells have been demonstrated to proliferate mainly in the liver, spleen and bone marrow and, in some cases, in the ovary and lymph nodes [14]. The observers were informed of this growth pattern in advance. First, the foci were localised using in vivo BLI images only, and then, visual evaluation was performed using in vivo BLI/FLI images including fusion images. When the predicted location was not changed by the addition of FLI, the observer recorded whether the confidence level of the judgement was improved or not. The locations determined visually were compared to those defined by ex vivo BLI to evaluate the accuracy of visual judgment.

Results

Serial in vivo FLI

We imaged live mice repeatedly from 1 h to 28 days after the intravenous injection of amino-PEG–QDs. Fluorescent signal intensity was elevated for the liver, spleen, skeleton and lymph nodes, indicating preferential uptake of amino-PEG–QD by the reticuloendothelial system (Fig. 1a). Visualisation of the skeleton was considered to be attributable to uptake by the bone marrow. Generally, contrast between the reticuloendothelial system and background regions tended to decrease over time (Fig. 1b), but patchy areas of strong fluorescence outside the reticuloendothelial systems were sometimes noted 1 h after injection. The liver was clearly visible even at 28 days post-injection, whereas the spleen was observed clearly up to 6 h but was almost undetectable at 14 days and later. The lower thoracic spine, lumbar spine, sacrum, sternum, humeri, femurs and tibias were identifiable even at 28 days post-injection. Scapulas, the anterior tips of the ribs, and iliac bones were faintly visible at the early time points. Within the skull, intense signals were found in the frontal bones and interparietal bone, presumably indicating that these bones have a relatively high bone marrow content. Fluorescence intensity was relatively strong in the proximal humeri and elbows within the anterior limbs and near the knee within the posterior limbs. The lymph nodes accumulated amino-PEG–QD more slowly than the liver, spleen and skeleton, and were visualised more clearly at 3 h or later than at 1 h. Inguinal, axillary and sacral nodes were identified in all mice, and popliteal nodes were visualised in two mice. Quantitative analysis demonstrated the strongest signal for the liver, spleen and spine 1 h post-injection and at 3 h for the inguinal lymph nodes (Fig. 1c). Prolonged retention of amino-PEG–QD in the reticuloendothelial system was confirmed quantitatively. No signs of toxicity caused by the amino-PEG–QD were apparent. Body weight measured at 1 day after injection was unchanged from that measured

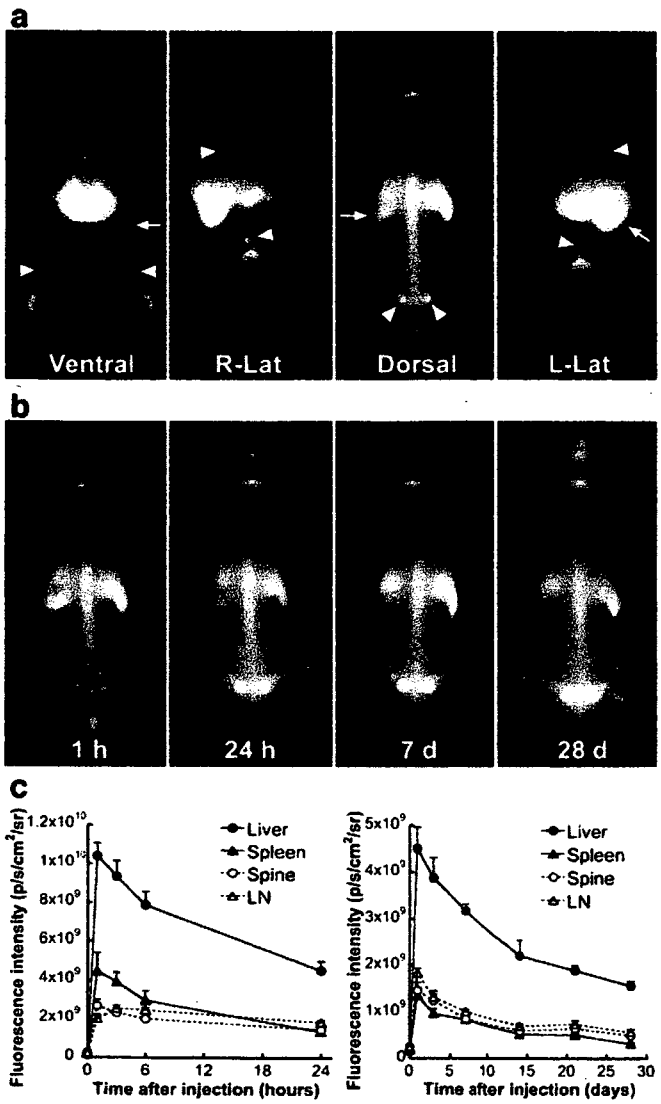

Fig. 1 In vivo FLI performed after intravenous injection of amino-PEG–QD. **a** Ventral, right-lateral (*R-Lat*), dorsal, and left-lateral (*L-Lat*) images obtained 3 h post-injection. The liver, spleen (*arrows*), skeleton, and lymph nodes (*arrowheads*) are visualised. The *grey* scale was adjusted for each image. **b** Dorsal images obtained at 1 h, 24 h, 7 days, and 28 days. The *grey* scale was optimized for each time point. Delineation of the lymph nodes is intensified at 24 h. Otherwise, the image contrast is higher at the earlier time points. **c** Temporal profiles of fluorescence intensity (left, up to 24 h; right, at 1, 3, 7, 14, 21, and 28 days) for the liver, spleen, spine, and inguinal lymph nodes (*LN*). *Error bars* indicate standard errors

before injection, and during the course of the study, the body weight was similar for mice that received QD and control mice that did not (data not shown).

Ex vivo FLI

The distribution of amino-PEG–QD was evaluated in detail 24 h after intravenous administration using ex vivo FLI. Quantitative analysis demonstrated that the strongest fluorescence was detected in the liver, followed by the spleen and spine, in mice injected with amino-PEG–QD (Fig. 2a). The contrast ratio, defined as the ratio of mean signal intensity in the QD-injected mice to that in control mice, was also largest for the liver (70.3 [standard deviation, 9.5]), followed by the spleen (30.0 [6.1]) and spine (14.9 [6.9]). A mild increase in fluorescence intensity was also noted for the lung (contrast ratio, 5.3 [2.4]). Although the signals for the stomach and intestine were relatively strong, they originated from gastrointestinal contents and were similar with or without QD injection. The kidney, heart, brain and femoral muscle showed weaker fluorescence than the lung after QD injection, and the contrast ratios for these organs were less than 2. Visual evaluation of the ovary, uterus and adrenal glands showed weak fluorescent signals, irrespective of QD injection. In mice injected with amino-PEG–QD, multiple small fluorescent spots were observed superficially and shown to correspond to superficial lymph nodes (Fig. 2b). Similar focal fluorescence was detected after removing the internal organs and was demonstrated to be derived from deep lymph nodes such as the paraaortic and iliac nodes. Intense lymph node signals were not observed in control mice. After removal of the internal organs and lymph nodes, intense fluorescence was observed in the skeleton of QD-injected mice only.

Longitudinal BLI/FLI

Five days after inoculation of Ba/F3–Luc/Wt cells, in vivo BLI demonstrated multiple bioluminescent foci in various regions, suggesting successful implantation. Seven days after inoculation, amino-PEG–QD were injected in the QD group, and in vivo BLI/FLI was performed about 3 h later. In vivo FLI visualised the liver, spleen, skeleton and lymph nodes, similar to imaging of mice without cell inoculation, and aided the localisation of bioluminescent signals (Fig. 3a). Fusion images helped to assess the relationship between bioluminescent foci and reticuloendothelial structures in detail. Mean whole-body bioluminescent signal intensities in the QD group were similar to those in the control group without QD injection (Fig. 3b), and no substantial effect of amino-PEG–QD on bioluminescent reaction was suggested. Imaging studies were then repeated weekly, which provided in vivo FLI images without any additional QD injection. Whole-body bioluminescent signals increased similarly between the two groups, suggesting no substantial effect of amino-PEG–QD on the proliferation of inoculated cells.

BLI/FLI assessment of lesion locations

We determined the locations of 52 bioluminescent foci in five mice inoculated with Ba/F3–Luc/Wt cells (Fig. 4).

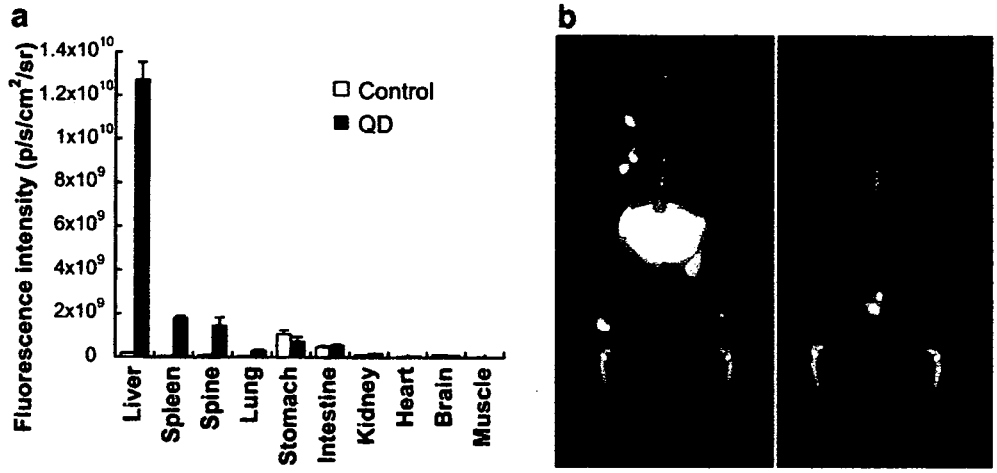

Fig. 2 Ex vivo FLI performed 24 h after intravenous injection of amino-PEG–QD. **a** Signal intensity measured for each organ in mice with (*QD*) and without (*control*) amino-PEG–QD injection. *Error bars* indicate standard errors. **b** Ventral fluorescent images obtained after removal of the skin and peritoneum (*left*) and subsequent removal of internal organs and anterior thoracic wall (*right*). The *left image* demonstrates focal fluorescence from superficial lymph nodes in addition to fluorescence from the skeleton, liver, and spleen. The intestinal fluorescence, originating from intestinal contents, is also observed. The *right image* shows focal signals from iliac lymph nodes

Based on ex vivo BLI, four lesions were judged to be present in the liver; four were found in the spleen, two in the ovary, six in the humerus, four in the sternum, eight in the rib, nine in the scapula, ten in the spine, two in the iliac bone and three in the femur. One observer, experienced in small animal imaging, accurately localised 44 foci using in vivo BLI alone and all 52 foci using in vivo BLI/FLI. Among the 44 foci localised accurately by both methods of visual evaluation, the confidence level was improved for 34 foci and unchanged for ten foci. The other observer who had less experience in small animal imaging accurately localised 34 foci using in vivo BLI alone and 50 foci using in vivo BLI/FLI. One hepatic focus was accurately localised using in vivo BLI but erroneously judged as a costal focus using in vivo BLI/FLI. Among the 33 foci localised accurately by both methods, confidence level was improved for 19 foci and unchanged for 14 foci.

Intense bioluminescent signals were observed around nine knees, and in vivo BLI/FLI enabled the distribution of the inoculated cells between the femur and tibia to be

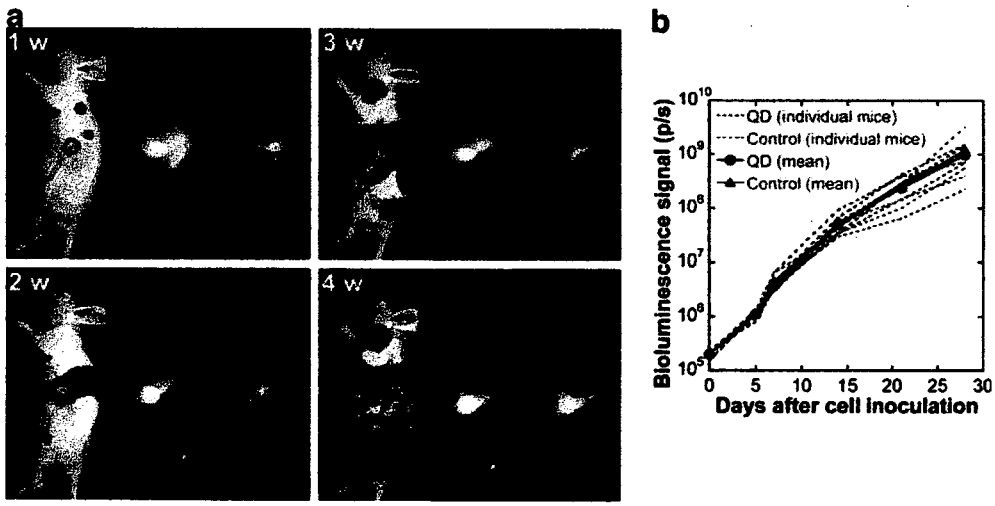

Fig. 3 Longitudinal BLI/FLI studies after inoculation of Ba/F3–Luc/Wt cells. The amino-PEG–QD and saline were administered in the QD group and the control group, respectively, 7 days after cell inoculation. **a** Left-lateral views of a mouse obtained at 1, 2, 3, and 4 weeks after cell inoculation. The *left image* for each week is the pseudo-colour bioluminescent image (*blue*, *green*, *yellow*, and *red* from the weakest to the strongest) overlaid on the *grey-scale photographic image*. The *middle image* is the grey-scale fluorescent image. The *right image* represents a fusion of the transparent, pseudo-colour bioluminescent image and the grey-scale fluorescent image. The scales for the bioluminescent and fluorescent images were adjusted for each time point. Bioluminescent foci were found in the liver at 1 week and, thereafter, developed in the spleen. Bone marrow involvement was also detected. At 4 weeks, extensive cell proliferation was seen in the liver, spleen, and bone marrow. Lymph nodes were not involved. **b** Time course of whole-body bioluminescent signal intensities in the QD group (*blue lines*) and controls (*red lines*). Data for individual mice (*dotted lines*) and mean values (*solid lines*) are presented

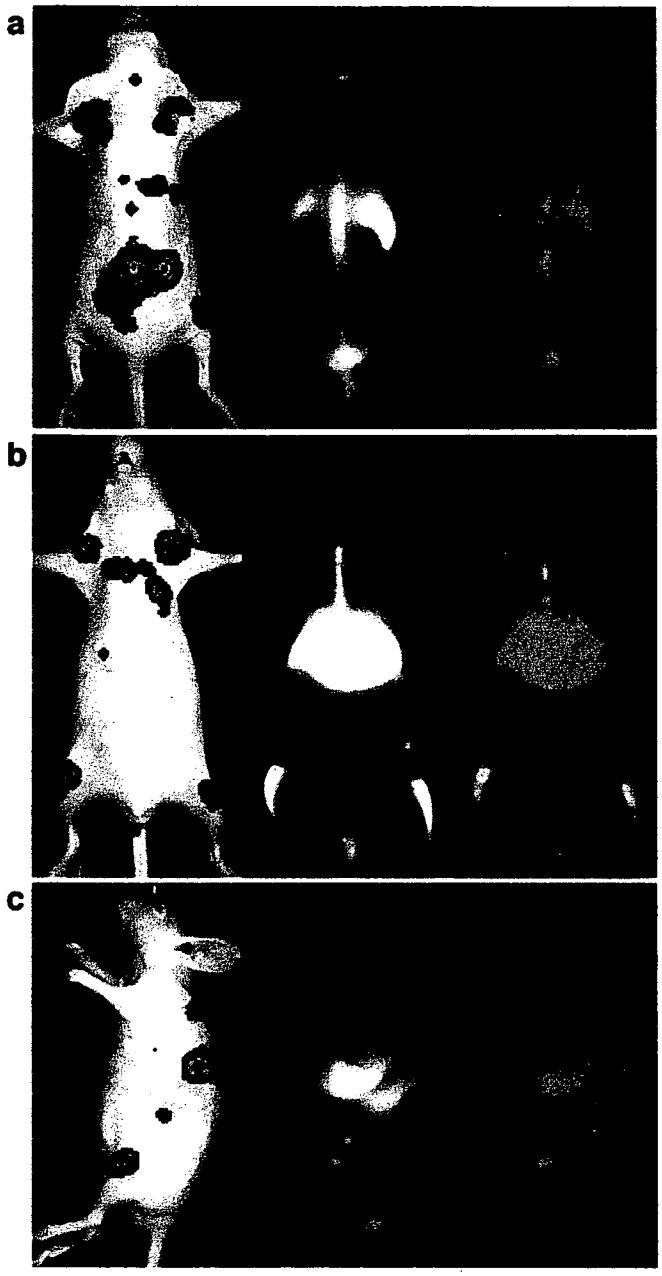

Fig. 4 Bioluminescent (*left*), fluorescent (*middle*), and fusion images (*right*) of mice inoculated with Ba/F3–Luc/Wt cells and injected with amino-PEG–QDs. **a** Dorsal images obtained 7 days after cell inoculation. Bioluminescent foci are shown in the lumbar spine, left iliac bone, right ovary, knees, thoracic spine, liver, scapulas, humeri, and interparietal bone. **b** Ventral images of the mouse presented in **a**. Bioluminescent foci are shown in proximal humeri, anterior tips of the ribs, sternum, liver, femurs, and tibias. **c** Left-lateral images obtained 9 days after cell inoculation. Bioluminescent foci are shown in the spleen, left femur, and left tibia. The focus on the dorsal portion of the chest was judged to be in the left scapula based on the dorsal images

assessed. The signals were shown to originate predominantly from the femur for four knees, predominantly from the tibia for one knee, and similarly from the femur and tibia for four knees. In the skeleton, bioluminescent foci were frequently located in areas showing strong fluorescent signals. Most bioluminescent foci in the neck were detected in proximal humeri, and most bioluminescent foci in the head were detected in the interparietal bone or frontal bone. Strong fluorescent signals were also seen in these areas. Fluorescent signals were relatively high at the anterior tips of the ribs, where bioluminescent foci were often found.

Discussion

It has been reported that the reticuloendothelial system of a mouse can be visualised non-invasively after QD injection [8]. In this study, we performed in vivo FLI on live mice after intravenous injection of amino-PEG–QD without targeting ligands and investigated the temporal patterns of QD distribution and the structures delineated on the acquired fluorescent images. Long-term, repeated imaging of the reticuloendothelial system was feasible after a single injection, and various bony structures and superficial lymph nodes were visualised in addition to the liver and spleen. Although a detailed assessment of toxicity was not performed, the appearances and body weights of the mice did not suggest any toxicity despite the prolonged retention of QD. These results indicate the utility of amino-PEG–QD for imaging of the reticuloendothelial system. Jackson et al. reported the lack of apparent acute toxicity in rats injected with higher doses of amino-PEG–QD (up to 50 pmol/g), supporting the safety of the agent [23]. Image contrast tended to be better at the earlier time points, and quantitative analysis also demonstrated stronger signals at these time points. However, 1 h after injection, patchy fluorescent signals were observed outside the reticuloendothelial structures, which may have been caused by extravasation of QD; in addition, the visualisation of lymph nodes was relatively obscure. The optimal time point for scanning was, therefore, found to be approximately 3–6 h after injection.

Selective accumulation of amino-PEG–QD in the reticuloendothelial system was confirmed by ex vivo FLI. The measurement was performed 24 h after injection, and contrast ratios would be higher at earlier time points. Superficial and deep lymph nodes were delineated as intense fluorescent spots. FLI using QD may serve as a guide when searching for lymph nodes during dissection. Although the upper thoracic spine was not visible on in vivo dorsal images, it was delineated on the ventral image acquired after removal of the internal organs and anterior thoracic wall. The presence of thick soft-tissues on the dorsal side of the upper thoracic spine appears to be responsible for the non-visualisation on in vivo images. Difficulty in assessing deep structures is a major limitation of optical imaging compared to X-ray imaging or MRI.

We attempted to use fluorescent reticuloendothelial imaging for the localisation of bioluminescent signals. In these experiments, mice were inoculated with model cells of a haematological malignancy that stably expresses firefly luciferase. First, we examined whether the administration of amino-PEG–QD affects the quantitative results of bioluminescent tumour monitoring. Alteration in bioluminescence intensity may be inferred to occur because of inhibition of the luciferase-dependent bioluminescent reaction, enhanced light attenuation in QD-containing tissues, changes in luciferase expression per cell, or variations in proliferative activity of the inoculated cells. However, whole-body bioluminescent signals were comparable between QD-injected mice and controls from 3 h to 3 weeks after QD injection, justifying the use of the FLI technique in quantitative bioluminescent tumour monitoring.

The intravenous administration of amino-PEG–QD enabled repeated localisation of bioluminescent foci on maps of the reticuloendothelial system and facilitated the identification of the structures harbouring the inoculated cells. Although even a single dose of QD offered useful anatomical information longitudinally, additional injection would improve the assessment of the relationship between bioluminescent foci and reticuloendothelial structures, especially spleen, in follow-up experiments. We determined the involved structures using ex vivo BLI [14, 20, 21] to evaluate the utility of combining FLI with bioluminescent tumour monitoring. In vivo BLI/FLI, accompanied by fusion of both images, improved the accuracy and confidence level of the localisation of the bioluminescent foci compared to BLI alone. Both BLI and FLI images were acquired using an identical CCD camera system with the mouse position unchanged, which made comparison between them easy and reliable. Fusion of the fluorescent and bioluminescent images was achieved without special data processing, and aided detailed interpretation of the relationship between bioluminescent foci and reticuloendothelial structures. An experienced investigator could usually predict the involved organ based on the photographic surface images. However, when a bioluminescent focus is present near the border between two structures, it is impossible to define the involved organ confidently. Alteration of organ morphology induced by disease progression may make the localisation more difficult in disease model animals. In addition, sub-optimal positioning of mice in the imaging chamber may prevent accurate localisation. Although a spinal lesion should be identified as a central focus on a dorsal image, it may be displaced because of distortion of the posture and may mimic a lesion in the liver, spleen or iliac bone. When two or more mice are examined simultaneously, mice placed in the peripheral area of the FOV are imaged in a somewhat oblique projection, and thus, it is difficult to determine the precise location of the spine. Fluorescent reticuloendothelial imaging using amino-PEG–QD would serve as a useful, convenient adjunct to BLI when the localisation of bioluminescent foci is desired.

In vivo BLI/FLI enabled the identification of bones containing inoculated cells. Determining the distribution of the inoculated cells among the bones may be beneficial for harvesting the cells for in vitro analysis. Skeletal bioluminescent foci were frequently demonstrated in areas showing intense fluorescent signals. It is suggested that bones with high bone marrow content accumulate amino-PEG–QD avidly and, at the same time, are susceptible to tumour cell implantation. FLI using amino-PEG–QD appears to aid in defining the distribution of bone marrow.

Combining X-ray imaging, CT or MRI with BLI can also add anatomical information to BLI [11–14]. However, FLI with amino-PEG–QD presents major advantages over other anatomical imaging methods, such as the wide availability and correct registration of bioluminescent and fluorescent images, as FLI can be performed immediately after BLI using the same CCD camera system. Moreover, BLI/FLI is neither time-consuming nor technically demanding. The FLI technique visualises the liver, spleen and lymph nodes in addition to the skeleton. Ionising radiation is not used, so the possible effects of radiation exposure on inoculated cells or host animals need not be considered. Disadvantages of FLI include difficulty in discriminating between overlapping organs because most in vivo FLI studies provide projectional images unlike CT or MRI. One hepatic focus was judged as a costal focus using in vivo BLI/FLI in this study, a misinterpretation that appears to be related to the overlap between the ribs and liver. Non-invasive FLI usually offers relatively low spatial resolution because of light scattering in the tissues. FLI with amino-PEG–QD visualises the reticuloendothelial organs only and cannot define other organs or tumour lesions directly. In animal models of haematological malignancies, lesions usually develop in the reticuloendothelial system, so the utility of FLI with amino-PEG–QD as anatomical landmarks appears to be high. The optimal anatomical imaging method should be selected for each experiment by considering the benefits of each method and the requirements of the experiment.

Although we injected 5 pmol/g amino-PEG–QD in this study, a dose of 2.5 pmol/g provided almost the same information soon after injection (data not shown). The appropriate injection dose remains to be defined, and it appears to depend on the CCD camera system, the fluorescent filters and the emission peak and surface coating of QD. We fused fluorescent and bioluminescent images using general-purpose software, and the use of dedicated software integrated into the data acquisition

system would improve the method in convenience. Intake of an alfalfa-free diet has been reported to reduce autofluorescence from the intestine [18]. Although we confirmed the beneficial effect of the alfalfa-free diet (data not shown) and provided the diet for at least 7 days before FLI, autofluorescence originating from intestinal contents remained relatively strong. Further modification of the diet may lead to a reduction in the required injection dose and improvement of the image quality.

In conclusion, we characterised in vivo fluorescent reticuloendothelial imaging using QD without targeting ligands and investigated its use in combination with in vivo BLI. The QD injected intravenously selectively accumulated in the reticuloendothelial system. Various structures were visualised soon after injection, and long-term repeated observation was possible without additional injections, although image contrast gradually decreased. No toxicity was indicated, and the intravenous administration did not affect quantitative results of bioluminescent tumour monitoring. Combining FLI using QD with BLI demonstrated the relationship between bioluminescent foci and reticuloendothelial structures and aided the localisation of bioluminescent foci. This combined imaging approach is practical and expected to allow bioluminescent tumour monitoring to yield more benefits.

Acknowledgment We thank Dr. Hiroshi Toyama, Department of Radiology, Fujita Health University, for the technical instruction. We also thank Mr. Norimasa Kitamura, Department of Radiology, Institute of Medical Science, University of Tokyo for the technical support. This work was supported in part by a Grant-in-Aid for Scientific Research from the Ministry of Education, Culture, Sports, Science and Technology of Japan.

References

1. Weissleder R. A clearer vision for in vivo imaging. Nat Biotechnol 2001;19:316–7.
2. Jaiswal JK, Simon SM. Potentials and pitfalls of fluorescent quantum dots for biological imaging. Trends Cell Biol 2004;14:497–504.
3. Medintz IL, Uyeda HT, Goldman ER, Mattoussi H. Quantum dot bioconjugates for imaging, labelling and sensing. Nat Matters 2005;4:435–46.
4. Hotz CZ. Applications of quantum dots in biology: an overview. Methods Mol Biol 2005;303:1–17.
5. Gao X, Cui Y, Levenson RM, Chung LW, Nie S. In vivo cancer targeting and imaging with semiconductor quantum dots. Nat Biotechnol 2004;22:969–76.
6. Cai W, Shin DW, Chen K, Gheysens O, Cao Q, Wang SX, et al. Peptide-labeled near-infrared quantum dots for imaging tumor vasculature in living subjects. Nano Lett 2006;6:669–76.
7. Kim S, Lim YT, Soltesz EG, De Grand AM, Lee J, Nakayama A, et al. Near-infrared fluorescent type II quantum dots for sentinel lymph node mapping. Nat Biotechnol 2004;22:93–7.
8. Ballou B, Lagerholm BC, Ernst LA, Bruchez MP, Waggoner AS. Noninvasive imaging of quantum dots in mice. Bioconjug Chem 2004;15:79–86.
9. Contag CH, Jenkins D, Contag PR, Negrin RS. Use of reporter genes for optical measurements of neoplastic disease in vivo. Neoplasia 2000;2:41–52.
10. Edinger M, Cao YA, Hornig YS, Jenkins DE, Verneris MR, Bachmann MH, et al. Advancing animal models of neoplasia through in vivo bioluminescence imaging. Eur J Cancer 2002;38:2128–36.
11. Minn AJ, Kang Y, Serganova I, Gupta GP, Giri DD, Doubrovin M, et al. Distinct organ-specific metastatic potential of individual breast cancer cells and primary tumors. J Clin Invest 2005;115:44–55.
12. Burch S, Bisland SK, Wilson BC, Whyne C, Yee AJ. Multimodality imaging for vertebral metastases in a rat osteolytic model. Clin Orthop Relat Res 2007;454:230–6.
13. Mouchess ML, Sohara Y, Nelson MD Jr, DeCLerck YA, Moats RA. Multimodal imaging analysis of tumor progression and bone resorption in a murine cancer model. J Comput Assist Tomogr 2006;30:525–34.
14. Inoue Y, Izawa K, Tojo A, Nomura Y, Sekine R, Oyaizu N, et al. Monitoring of disease progression by bioluminescence imaging and magnetic resonance imaging in an animal model of hematologic malignancy. Exp Hematol 2007;35:407–15.
15. Inoue Y, Tojo A, Sekine R, Soda Y, Kobayashi S, Nomura A, et al. In vitro validation of bioluminescent monitoring of disease progression and therapeutic response in leukaemia model animals. Eur J Nucl Med Mol Imaging 2006;33:557–65.
16. Copelan EA, McGuire EA. The biology and treatment of acute lymphoblastic leukemia in adults. Blood 1995;85:1151–68.
17. Li S, Ilaria RL Jr, Million RP, Daley GQ, Van Etten RA. The P190, P210, and P230 forms of the BCR/ABL oncogene induce a similar chronic myeloid leukemia-like syndrome in mice but have different lymphoid leukemogenic activity. J Exp Med 1999;189:1399–412.
18. Troy T, Jekic-McMullen D, Sambucetti L, Rice B. Quantitative comparison of the sensitivity of detection of fluorescent and bioluminescent reporters in animal models. Mol Imaging 2004;3:9–23.
19. Lim YT, Kim S, Nakayama A, Stott NE, Bawendi MG, Frangioni JV. Selection of quantum dot wavelengths for biomedical assays and imaging. Mol Imaging 2003;2:50–64.
20. Jenkins DE, Oei Y, Hornig YS, Yu SF, Dusich J, Purchio T, et al. Bioluminescent imaging (BLI) to improve and refine traditional murine models of tumor growth and metastasis. Clin Exp Metastasis 2003;20:733–44.
21. Yoshimitsu M, Sato T, Tao K, Walia JS, Rasaiah VI, Sleep GT, et al. Bioluminescent imaging of a marking transgene and correction of Fabry mice by neonatal injection of recombinant lentiviral vectors. Proc Natl Acad Sci U S A 2004;101:16909–14.
22. Inoue Y, Izawa K, Tojo A, Sekine R, Okubo T, Ohtomo K. Light emission requires exposure to the atmosphere in ex vivo bioluminescence imaging. Mol Imaging 2006;5:53–6.
23. Jackson H, Muhammad O, Daneshvar H, Nelms J, Popescu A, Vogelbaum MA, et al. Quantum dots are phagocytized by macrophages and colocalize with experimental gliomas. Neurosurgery 2007;60:524–9.

Bone Marrow Transplantation (2007) 00, 1–6

www.nature.com/bmt

ORIGINAL ARTICLE

Preemptive therapy with ganciclovir 5 mg/kg once daily for cytomegalovirus infection after unrelated cord blood transplantation

A Tomonari[1], S Takahashi[1], J Ooi[1], N Tsukada[1], T Konuma[1], T Kobayashi[1], K Takasugi[1], T Iseki[1], A Tojo[1] and S Asano[1,2]

[1]*Department of Hematology/Oncology, The Institute of Medical Science, The University of Tokyo, Tokyo, Japan and* [2]*Integrative Bioscience and Biomedical Engineering, School of Science and Engineering, Waseda University, Tokyo, Japan*

The efficacy and safety of preemptive therapy using ganciclovir (GCV) 5 mg/kg once daily for CMV infection after unrelated cord blood transplantation (CBT) were studied. The initial preemptive therapy with GCV 5 mg/kg once daily led to resolution of CMV antigenemia in 25 of 34 patients (74%). In the remaining 9 patients (26%), antigenemia resolved after dose-escalation of GCV or change to foscarnet therapy. Recurrence of antigenemia was seen in 18 patients (53%). A total of 12 patients received the second preemptive therapy with GCV 5 mg/kg once daily, which led to resolution of antigenemia in 11 of 12 patients (92%). The remaining 1 patient (8%) required change to foscarnet therapy. None of 34 patients developed CMV disease. Neutropenia with an absolute neutrophil number of less than 1 and 0.5×10^9 per liter after GCV therapy occurred in 12 (35%) and 1 (3%) patients, respectively, after the initial therapy, and in 2 (17%) and 0 (0%) patients, respectively, after the second therapy. No patients developed neutropenic fever or secondary graft failure after GCV therapy. There were no deaths directly attributable to GCV therapy. The present study suggests that antigenemia-based preemptive strategy using GCV 5 mg/kg once daily is feasible and effective for CBT recipients.
Bone Marrow Transplantation (2007) 0, 000–000. doi:10.1038/sj.bmt.1705910
Keywords: preemptive therapy; CMV; ganciclovir; neutropenia; cord blood transplantation

Introduction

CMV disease is one of the major infectious complications after allogeneic hematopoietic SCT.[1,2] By applying various surveillance methods such as antigenemia and PCR assays, preemptive strategies with ganciclovir (GCV) have been widely used for preventing early CMV disease after SCT. In most preemptive strategies, GCV is administered intravenously at a dose of 5 mg/kg twice daily as an initial induction phase for 1–2 weeks, then followed by 6 mg/kg once daily as a maintenance phase.[3] One of the major adverse effects of GCV is neutropenia.[4] In an attempt to reduce the incidence of GCV-related neutropenia, preemptive therapy with GCV 5 mg/kg once daily has previously been used as initial induction therapy for BMT and peripheral blood SCT (PBSCT) recipients.[5–7] The favorable outcomes suggested that this strategy could reduce the incidence of GCV-related neutropenia but retained the efficacy for preventing CMV disease in BMT and PBSCT recipients.

Umbilical cord blood transplantation (CBT) from an unrelated donor has recently been utilized as an alternative therapy for patients who do not have suitable donors for BMT or PBSCT.[8,9] Previous studies have shown that CMV infection occurs frequently in adult patients after CBT.[10,11] In addition, patients with CMV infection after CBT have a higher probability of secondary graft failure than those without CMV infection.[11] Toxicity of GCV may be associated with secondary graft failure in CBT recipients with CMV infection.

In our previous study, we reported the results of antigenemia-based preemptive GCV therapy for CMV infection in adult patients after unrelated CBT.[12] The preemptive therapy consisted of GCV 5 mg/kg twice daily as an initial induction phase for 2 weeks and 5 mg/kg once daily as a maintenance phase for 1 week or more. Because of recent favorable outcomes in BMT and PBSCT recipients, we examined the efficacy and toxicity of preemptive therapy using GCV 5 mg/kg once daily for CMV infection after unrelated CBT in the present study.

Patients and methods

Patients

Between May 2002 and April 2006, 60 patients underwent CBT using a conditioning regimen containing 12 Gy total body irradiation. Among them, 34 patients who developed CMV antigenemia and initially received preemptive ther-

Correspondence: Dr A Tomonari, Department of Hematology/Oncology, The Institute of Medical Science, The University of Tokyo, 4-6-1, Shirokanedai, Minato-ku, Tokyo 108-8639, Japan.
E-mail: atomonar@ims.u-tokyo.ac.jp
Received 20 April 2007; revised 28 August 2007; accepted 24 September 2007

Gml : Ver 6.0
Template: Ver 1.1.3
Journal: BMT ☐ Disk used Despatch Date: 10/10/2007
Article : NPG_BMT_1705910 Pages: 1–6 OP: bvr